

Modeling of high-strength steels (HSS) in automobile forming

COE-C3010 - Computational Engineering Project 2024 - Aalto University

Group 5: An Mai, Hoang Le, Linh Nguyen, Thoa Le

Advisor: Li Zinan

Supervisor: Junhe Lian

Table of Contents

| | |
|---|-----------|
| Abstract..... | 1 |
| 1 Introduction | 2 |
| 2 Literature Review..... | 4 |
| 2.1 Constitutive model approach..... | 4 |
| 2.1.1 Swift-Voce law..... | 4 |
| 2.1.2 Evolving Non-Associated Hill48 Model | 6 |
| 2.2. Long Short-Term Memory (LSTM)..... | 9 |
| 2.1.1. An overview of LSTM..... | 9 |
| 2.1.2. LSTM application in predicting flow curve | 12 |
| 2.1.3. Evaluation of LSTM model using Mean Squared Error (MSE) | 13 |
| 3. Methodology..... | 15 |
| 3.1. Constitutive model..... | 15 |
| 3.1.1. Flow curve fitting with Swift – Voce equation | 15 |
| 3.1.2. Temperature dependency function parameter calibration | 15 |
| 3.1.3. Strain-rate dependency function parameter calibration | 20 |
| 3.2. Machine Learning-based model: Long Short-Term Memory | 26 |
| 3.2.1. Data preprocessing | 26 |
| 3.2.2. Model Architecture and Implementation | 26 |
| 3.3. Validation | 28 |
| 4. Results & Discussion | 30 |
| 4.1. Constitutive model..... | 30 |
| 4.1.1. Flow curve fitting with Swift – Voce equation | 30 |
| 4.1.2. Temperature dependency function parameter calibration | 32 |
| 4.1.3. Strain-rate dependency function parameter calibration | 43 |
| 4.2. Long Short-Term Memory model | 50 |
| 4.3. Validation | 54 |
| 4.3.1. Machine Learning model..... | 54 |
| 4.3.2. Constitutive Model..... | 55 |
| 4.4. Comparison between constitutive model and LSTM model | 59 |
| 5. Conclusions and Outlooks | 61 |
| 6. Personal evaluation..... | 63 |
| References..... | 64 |
| Appendix | 66 |

Abstract

This project aims to develop and validate temperature- and strain-rate-dependent models for high-strength steel (HSS) used in automobile forming processes. With the increasing demand for lightweight components and improved crashworthiness in the automotive industry, it is essential to model the behavior of HSS during forming. The hot forming process, known for producing parts with optimal material behavior, is highly influenced by temperature and strain-rate conditions. The project focuses on utilizing the isotropic hardening rule for plasticity, incorporating both temperature and strain-rate dependencies. The study includes literature research on parameter identification methods and different polynomial functions for fitting thermal and strain-rate dependency functions. Two models are developed: one based on an existing temperature dependency function and the other using a proposed function that provides better fitting accuracy. The project also involves optimizing parameters and validating the models under various thermal and strain-rate conditions. Finally, the models are validated to ensure their predictive capability in real-world forming scenarios. In addition to the traditional constitutive models, a machine learning (ML)-based approach is explored as a secondary method to compare with the established models. This ML model is constructed using code provided by the advisor, aiming to predict material behavior based on experimental data. Although the primary focus is on the development and validation of the constitutive models, the comparison with the ML model provides additional insights into its potential advantages and limitations in predicting HSS behavior under varying conditions. The key learning outcomes include gaining knowledge of material modeling, applying programming skills, and developing scientific writing for research documentation. The final deliverables will consist of optimized functions, a local Python repository with developed scripts, and an instructional tutorial. A joint report and public presentation will summarize the findings, contributing to a deeper understanding of HSS material behavior in automobile forming applications.

1 Introduction

In recent years, the application of high-strength steels (HSS) in the automotive industry has transformed vehicle design and manufacturing. These advanced materials allow engineers to design lighter, safer, and more efficient vehicles by balancing lightweight construction with crashworthiness. As safety and environmental concerns continue to grow, HSS has become increasingly essential for meeting regulatory and performance standards. However, achieving optimal performance in HSS parts during automotive forming processes requires a precise understanding of the material's behaviour under varied temperature and strain-rate conditions. This project aims to develop a model capable of accurately simulating material DP1000 flow curves and fracture points under different conditions to optimize forming processes and predict material behaviour under operational stresses. In this project, two different approaches to modelling are examined: the constitutive model's parameters calibration approach with finite element method (FEM) and artificial intelligence approach with Long Short-Term Memory (LSTM).

Finite Element Method (FEM) is a powerful numerical technique that divides complex structures into smaller, manageable finite elements, enabling detailed analysis of stress, strain, and deformation within materials. The strengths of FEM lie in its ability to incorporate detailed material properties and boundary conditions, offering physical insights into material behaviour. However, FEM can be computationally intensive and time-consuming, requiring precise material data for calibration. In this project, we derive the flow curves from the existing FEM models of different specimen and the experimental data with numerical method optimization for Swift-Voce equations. The flow curves are then validated by the force-displacement prediction with simulation. Along with flow curve prediction, the parameters of Uncoupled Modified Bai-Wierzbicki (MBW) model are calibrated based on parameter identification methods to fit with the strain-rate dependent and temperature dependant material behaviours. Finally, the predicted flow curve is used to validate the calibrated parameters to arrive at the final parameters for DP1000.

Introduction

On the other hand, LSTM networks is well-suited for modelling sequential and time-dependent data. The advantages of using LSTM include its ability to model complex, non-linear relationships without explicitly defining the underlying physical laws, reducing the need for extensive material characterization. However, this method relies heavily on the availability of large and diverse datasets and may lack the interpretability of physics-based models like FEM. The "black box" nature of neural networks makes it challenging to understand the underlying mechanisms driving the predictions and valuable insights on the material are lost. Applying LSTM to DP1000 steel in this project involves training the network on existing experimental data to predict flow curves and fracture points under different forming conditions.

Following this section, the report discusses the theoretical background and literature review in section 3, covering topics such as the Swift-Voce law, the MBW model and LSTM. Section 4 describes the methodology for FEM and LSTM approaches. Section 5 is the result and section 6 are the discussion where the different methods are compared. Section 7 is the conclusion and outlooks of the project. Finally, section 8 covers the personal and course evaluation from our group.

2 Literature Review

This section covers the theoretical background for Constitutive model and LSTM approaches. For the constitutive model method, see section 3.1. For LSTM method, see section 3.2.

2.1 Constitutive model approach

2.1.1 Swift-Voce law

The Swift-Voce equation defines the plastic deformation behavior in materials by combining Swift hardening law which describes the hardening behavior and Voce law which describes the stress-strain behaviors.

$$\sigma_{S-V_y}(\varepsilon_p) = \alpha \cdot A(\varepsilon_0 + \varepsilon_p)^n + (1 - \alpha) \cdot [k_0 + Q(1 - e^{-\beta_0 \varepsilon_p})] \quad (2-1)$$

In equation (2-1), $\sigma_{S-V_y}(\varepsilon_p)$ is the yield stress as function of plastic strain and α is the weighing factor of Swift and Voce law.

The Swift law (Swift, 1952) is expressed as

$$\sigma_S(\varepsilon_p) = A(\varepsilon_0 + \varepsilon_p)^n \quad (2-2)$$

Where:

- $\sigma_S(\varepsilon_p)$ is the true stress
- A is the material strength coefficient
- ε_0 is a pre-strain or offset strain
- ε_p is the true plastic strain
- n is the strain hardening exponent

The Voce law is expressed as

$$\sigma_{V_y}(\varepsilon_p) = k_0 + Q(1 - e^{-\beta_0 \varepsilon_p}) \quad (2-3)$$

Where:

- $\sigma_{V_y}(\varepsilon_p)$ is the true stress
- k_0 is the initial yielding stress before hardening
- Q is the saturation stress
- β_0 is a parameter that controls how quick stress approaches saturation
- ε_p is the true plastic strain

The true stress and strain are obtained from experiment while $A, \varepsilon_0, \varepsilon_p, k_0, Q, \beta_0, \alpha$ need to be determined for a specific material usually by uniaxial tension tests. After

calibration, more stress and strain data can be generated from the equation and used as the input for simulation.

The Swift-Voce equation has shown good results when fitted for low strain-rate. However, for higher strain-rate such as 1, the modified Swift-Voce equation has shown better results since it accounts for initial rapid hardening, saturation effects, and additional damping. The modified Swift-Voce equation can be described in Equation (2-4).

$$\sigma_{MSV}(\varepsilon) = A \cdot (\varepsilon + \varepsilon_0)^n + Q \cdot (1 - e^{-B \cdot \varepsilon}) \cdot \frac{1 - e^{-\alpha \cdot \varepsilon}}{1 + \beta \cdot \varepsilon} \quad (2-4)$$

Where the Swift equation is kept the same as described in Equation (2-2), the Voce equation is updated in Equation (2-5) and the new damping term is shown in Equation (2-6).

Modified Voce equation:

$$\sigma_{Voce}(\varepsilon) = Q \cdot (1 - e^{-B \cdot \varepsilon}) \quad (2-5)$$

Where:

- $\sigma_{Voce}(\varepsilon)$ is the true stress
- Q is the saturation stress
- B is a parameter that controls how quick stress approaches saturation
- ε is the true plastic strain

Damping term:

$$\text{Damping} = \frac{1 - e^{-\alpha \cdot \varepsilon}}{1 + \beta \cdot \varepsilon} \quad (2-6)$$

Where:

- α is the rate of exponential damping
- β influences how the damping effect scales with strain
- ε is the true plastic strain

To achieve the best fitting quality, the parameters should be validated by comparing the difference in the force – displacement curve between experiment and simulation and modified accordingly.

For material DP1000, these parameters have been calibrated at room temperature (RT, 25 °C) and quasi-static (QS, 0.0001 s–1) tensile test result and shown good fitting

quality in comparison to using only Swift or Voce law for flow curve derivation. The result can be seen in Table 2-1 (Liu et al., 2019).

Table 2-1: Hardening parameters for DP1000 (RT, QS).

| A | ε_0 | n | k_0 | Q | β_0 | α |
|------|-----------------|-------|--------|--------|-----------|----------|
| 1300 | $2.3e^{-14}$ | 0.075 | 773.28 | 266.19 | 73.94 | 0.5 |

2.1.2 Evolving Non-Associated Hill48 Model

The model used to run the simulation in this study is the evolving non-associated Hill48 models proposed by Lian et al. (2018). This model represents a significant advancement in the field of plasticity modeling, particularly for materials exhibiting anisotropic behavior. These models extend the traditional Hill48 plasticity framework by incorporating non-associated flow rules and evolving characteristics of material properties, such as the r-value, which addresses the inaccuracy of the traditional model (Shen et al., 2020). The traditional Hill48 model assumes associated flow rules, where the yield surface and plastic potential are linked. However, many materials do not conform to this assumption, requiring the development of non-associated models. This approach decouples the yield function from the plastic potential function, introducing greater complexity and flexibility in material modeling (Shen et al., 2018). The Table 2-2 summarizes key differences between these two models.

Table 2-2: Comparison of the associated and evolving non-associated Hill48 models.

| | Associated Flow Rule | Non-Associated Flow |
|----------------------------|--|--|
| Yield & potential Function | identical | distinct |
| Plastic flow direction | aligned with yield surface | differ from yield surface |
| Complexity | simple, less flexible | complex, flexible |
| Material behavior | isotropic materials (Chahaoui et al., 2021) | anisotropic materials (Shen et al., 2018) |

The yield function f and flow potential function g of the evolving non-associated Hill48 model are defined by the following equations:

$$f = \bar{\sigma}(\alpha_{i \sim j}, \sigma) - \sigma_Y(\bar{\varepsilon}^p) \leq 0 \quad (2-7)$$

$$g = \bar{\sigma}(\beta_{i \sim j}, \sigma) - \sigma_Y(\bar{\varepsilon}^p) \leq 0 \quad (2-8)$$

Where:

- $\bar{\sigma}$ is equivalent stress with $\alpha_{i \sim j}$ and $\beta_{i \sim j}$ as anisotropic parameters and $\sigma_Y(\bar{\varepsilon}^p)$ as reference stress state.

Flow rule:

$$\dot{\varepsilon}^p = \lambda * \frac{\partial g}{\partial \sigma} \quad (2-9)$$

Where:

- $\dot{\varepsilon}^p$ is equivalent plastic strain-rate tensor.
- λ is a scalar factor with non-negative values used for updating the plastic strain-rate tensor.

In this model, the equivalent stress is governed by a simple quadratic expression to describe the three-dimensional anisotropy.

$$\bar{\sigma}(\alpha_{i \sim j}, \sigma) = \left\{ \frac{1}{2} [F_\sigma(\sigma_{22} - \sigma_{33})^2 + G_\sigma(\sigma_{33} - \sigma_{11})^2 + H_\sigma(\sigma_{11} - \sigma_{22})^2] + L_\sigma \sigma_{23}^2 + M_\sigma \sigma_{13}^2 + N_\sigma \sigma_{12}^2 \right\}^{\frac{1}{2}} \quad (2-10)$$

$$\bar{\sigma}(\beta_{i \sim j}, \sigma) = \left\{ \frac{1}{2} [F_r(\sigma_{22} - \sigma_{33})^2 + G_r(\sigma_{33} - \sigma_{11})^2 + H_r(\sigma_{11} - \sigma_{22})^2] + L_r \sigma_{23}^2 + M_r \sigma_{13}^2 + N_r \sigma_{12}^2 \right\}^{\frac{1}{2}} \quad (2-11)$$

Where:

- $F_\sigma, G_\sigma, H_\sigma, L_\sigma, M_\sigma$, and N_σ are anisotropic parameters related to the anisotropic parameter $\alpha_{i \sim j}$ in the yield function.
- F_r, G_r, H_r, L_r, M_r , and N_r are anisotropic parameters related to the anisotropic parameter $\beta_{i \sim j}$ in the potential flow function.

These parameters are calibrated independently using experimental results obtained from uniaxial and biaxial tensile test data, represented by the flow stress at rolling directions, diagonal, transverse, and biaxial direction. The r-values (known as Lankford coefficients) in this model refer to the material ability to deform in thickness versus its ability to deform in the planar directions. Equations (2-12) to (2-15) are derived from Shen et al., 2020.

$$F_\sigma = \frac{\sigma_0^2(\overline{\epsilon^P})}{\sigma_{90}^2(\overline{\epsilon^P})} - 1 + \frac{\sigma_0^2(\overline{\epsilon^P})}{\sigma_b^2(\overline{\epsilon^P})} \quad F_r = \frac{2r_o(\overline{\epsilon^P})}{r_{90}(\overline{\epsilon^P})(1 + r_o(\overline{\epsilon^P}))} \quad (2-12)$$

$$G_\sigma = 1 - \frac{\sigma_0^2(\overline{\epsilon^P})}{\sigma_{90}^2(\overline{\epsilon^P})} + \frac{\sigma_0^2(\overline{\epsilon^P})}{\sigma_b^2(\overline{\epsilon^P})} \quad G_r = \frac{2}{1 + r_o(\overline{\epsilon^P})} \quad (2-13)$$

$$H_\sigma = 1 + \frac{\sigma_0^2(\overline{\epsilon^P})}{\sigma_{90}^2(\overline{\epsilon^P})} - \frac{\sigma_0^2(\overline{\epsilon^P})}{\sigma_b^2(\overline{\epsilon^P})} \quad H_r = \frac{2r_o(\overline{\epsilon^P})}{1 + r_o(\overline{\epsilon^P})} \quad (2-14)$$

$$N_\sigma = \frac{4\sigma_0^2(\overline{\epsilon^P})}{\sigma_{45}^2(\overline{\epsilon^P})} - \frac{\sigma_0^2(\overline{\epsilon^P})}{\sigma_b^2(\overline{\epsilon^P})} \quad Nr = \frac{\left(r_{90}(\overline{\epsilon^P}) + r_o(\overline{\epsilon^P})\right)\left(1 + 2r_{45}(\overline{\epsilon^P})\right)}{r_{90}(\overline{\epsilon^P})(1 + r_o(\overline{\epsilon^P}))} \quad (2-15)$$

Where:

- σ_0 , σ_{45} , σ_{90} , and σ_b are the stresses for uniaxial tensile tests along rolling directions, diagonal, transverse, and biaxial tensile test.
- r_0 , r_{45} , r_{90} , and r_b are r-values for uniaxial tensile tests along rolling directions, diagonal, transverse, and biaxial tensile test.

2.2. Long Short-Term Memory (LSTM)

2.1.1. An overview of LSTM

A Recurrent Neural Networks (RNN) is a deep neural network trained on sequential or time series data to create a machine learning (ML) model that can make sequential predictions or conclusions based on sequential inputs" (Stryker, 2024). The decision-making principle of RNN is that the model maintains a hidden state which captures information about previous inputs and uses them to make decision for the next node. However, standard RNNs struggle with long-term dependencies due to issues such as vanishing and exploding gradients during training. This limitation makes RNNs ineffective for model sequences where significant information from earlier steps affects later outputs.

Long Short-Term Memory (LSTM) Networks were introduced to address these challenges (Hochreiter and Schmidhuber, 1997). LSTMs are a special kind of RNN capable of learning long-term dependencies by incorporating a memory cell and gating mechanisms that regulate information flow. The core components of LSTM networks are the cell state (cell state, candidate cell state and hidden state), the gates (forget gate, input gate and output gate). The information flow between the cells and gates are controlled by activation function. For the forget gate, input gate, and output gate, the activation function is sigmoid (σ). The cell state is generated and the hidden state is updated by the Hyperbolic Tangent ($tanh$) function. These activation functions are important to the network since they introduce nonlinearity which allows the network to learn complex, nonlinear relationships and maintain gradients during backpropagation, which is essential for effective learning.

The sigmoid function (see equation (2-16)) outputs values between 0 and 1. In the network, it acts as a gate by deciding how much information to let through: A value of 0 blocks information while a value of 1 allows all information to pass. The sigmoid function is useful because it can represent probabilities and proportions, indicating how much of the information should pass through. For example, in the forget gate, it determines the fraction of the previous cell state to forget.

$$\sigma(x) = \frac{1}{1 + e^{-x}} \quad (2-16)$$

The Hyperbolic Tangent function (see equation (2-17)) outputs values between -1 and 1 and has a central distribution around 0. It allows the network to model a wider range of data by providing a way to introduce both positive and negative values. In the candidate cell state, it generates new potential content to add to the cell state. In the hidden state, it decides the final output of the LSTM cell by modulating the cell state.

$$\tanh(x) = \frac{e^x - e^{-x}}{e^x + e^{-x}} \quad (2-17)$$

Figure 2-1 describes the information flow and how the cell states are updated in an LSTM block. The specific equations used for calculating gate's value can be found below.

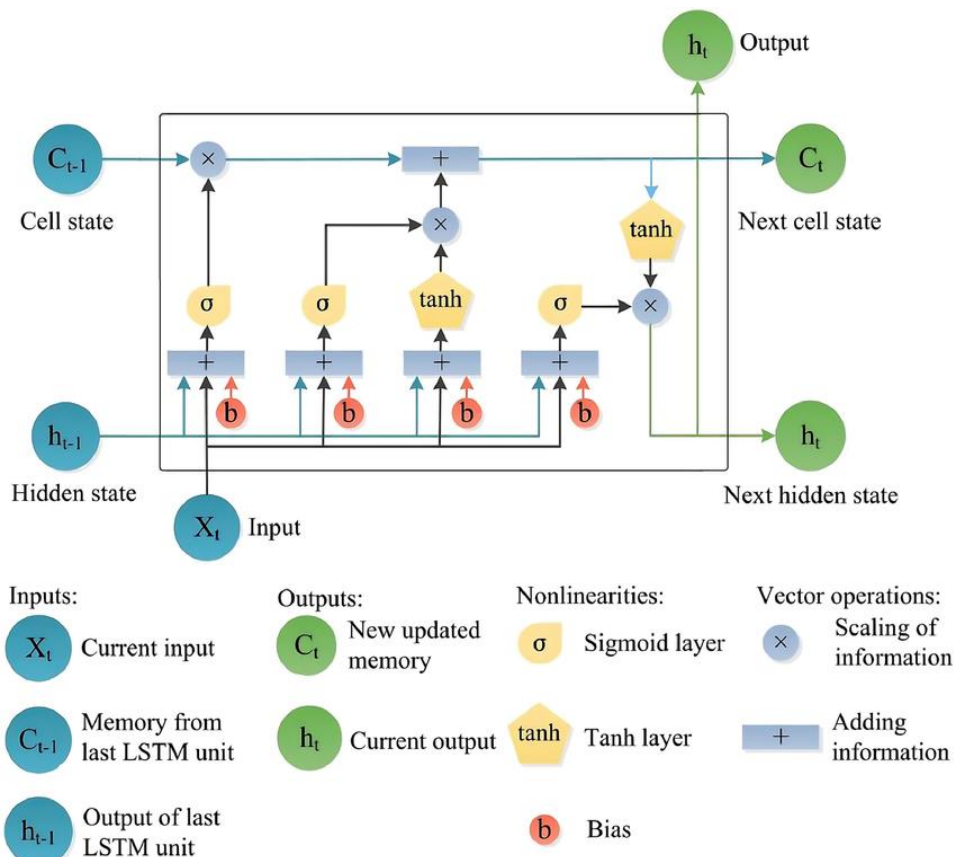


Figure 2-1: LSTM block breakdown. (Tian et al. 2021)

- The cell state (C_t) acts as the memory of the network, carrying information across time steps. The cell state allows the LSTM to retain or forget information as needed.
- The forget gate (f_t) decides what information to discard from the cell state. It uses a sigmoid function to output a value between 0 and 1 for each piece of information in the cell state.

$$f_t = \sigma(W_f \cdot [h_{t-1}, x_t] + b_f) \quad (2-18)$$

where

- o h_{t-1} is the previous hidden stage. It encapsulates the sequence's history up to time $t - 1$ to inform the network about the previous time step, which allows LSTM to maintain temporal dependencies and patterns over time.
- o x_t is the input at time t . It introduces new information to the network, which together with h_{t-1} , affects the gate activations and subsequent computations within the cell.
- o W_f is the weight matrix that dictate how much influence each element of h_{t-1} and x_t has on the forget gate f_t . During training, the network adjusts W_f to minimize the loss function and find the optimal weights for accurate predictions.
- o b_f is the bias for the forget gate. It adjusts the weighted sum before the activation function is applied and thereby improves the model's ability to learn by allowing it to shift activation thresholds, increasing its capacity to fit complex patterns in the data.
- The input gate (i_t), together with some candidate values (\tilde{C}_t), determines which new information to add to the cell state.

$$i_t = \sigma(W_i \cdot [h_{t-1}, x_t] + b_i) \quad (2-19)$$

$$\tilde{C}_t = \tanh(W_C \cdot [h_{t-1}, x_t] + b_C) \quad (2-20)$$

- Finally, the output gate controls the output based on the updated cell state.

$$o_t = \sigma(W_o \cdot [h_{t-1}, x_t] + b_o) \quad (2-21)$$

When new input flow in, the network updated the cell state and compute the new hidden stage as in equation (2-22).

$$C_t = f_t \odot C_{t-1} + i_t \odot \tilde{C}_t \quad (2-22)$$

$$h_t = o_t \odot \tanh(C_t) \quad (2-23)$$

2.1.2. LSTM application in predicting flow curve

LSTM networks have become increasingly popular in material science since many processes such as deformation, phase transformation, and damage evolution are inherently time-dependent and influenced by the previous states (Mozaffar et al., 2019). By applying this method, scientist can achieve accurate prediction from experimental sequential data without the need to explicitly program the underlying physical laws (Goodfellow et al., 2016). For example, LSTMs have been used to model microstructural evolutions (Sase and Shibuta, 2023) or simulate path-dependent plasticity in metals (Gorji et al., 2020). Among these applications, the LSTM network is particularly useful for predicting flow curves of high-strength steel, which involves modeling the material's response under various strains, strain-rates, and temperatures. In this application, LSTM networks can learn the relationship between the parameters and the flow stress from the experimental data and ultimately predict the stress when experiment cannot be performed.

One of the key advantages of using LSTM networks in predicting flow curves is their ability to handle the non-linear relationships in material deformation. The stress-strain relationship is non-linear since the material behavior during deformation is influenced by strain hardening, dynamic recovery, and phase transformations. LSTM networks can capture this relationship without linear approximations that are typically required in traditional empirical models (Benabou, 2021). Additionally, LSTM networks can produce excellent time-series prediction. In plastic deformation, the current state of the material depends on the history of stress and strain. By employing LSTMs, these temporal dependencies can be captured without correlation study or parameter identification (Dabbagh et al., 2024). This capability is important for materials that have rate-dependent behaviors or where the deformation history significantly influences the material behavior. Moreover, LSTM models can predict the flow curve effectively even with small datasets. In material science research, obtaining large datasets from

experiment can be expensive and time-consuming. By controlling the information flow with the forget gate and activation functions, LSTMs can extract meaningful patterns and makes a practical tool for projects that have limited experimental data available.

On the other hand, there are some aspects that should be considered when applying LSTM models to predict flow curves. A critical issue is the data quality since the accuracy of LSTM predictions relies heavily on the quality and representativeness of the training data. If the dataset is incomplete or noisy, the model cannot generalize and produce inaccurate predictions under varying conditions (Moradkhani et al., 2023). Therefore, to build a robust model, the dataset must capture the full range of deformation behaviors and conditions. For example, the material should be tested under different temperatures, strains and strain-rates. Another consideration is overfitting. Overfitting occurs when a model learns the training data too well, including its noise and outliers, which adversely affects its performance on unseen data. This problem typically happens when the dataset is too small, but it can be mitigated by cross-validation and by tuning the model complexity to match the size (Benabou, 2021). Finally, even though the models can predict the flow curve accurately, it is difficult to gain insights into material behavior with LSTM networks. Deep learning techniques are often considered a “black box” which means that the internal decision-making mechanism is not easy to understand (Pillai et al., 2021). Nevertheless, understanding the relationship between variables is crucial in material science since it allows scientists to hypothesize new physical models and theories. To address this issue, LSTM models should be accompanied with physics-based models or interpretation techniques such as attention mechanisms.

All in all, even though the LSTM network has some limitations, it is a powerful and convenient tool for scientists to explore the material’s behavior without expensive experiments or time-consuming modeling and simulations.

2.1.3. Evaluation of LSTM model using Mean Squared Error (MSE)

MSE is a commonly used metric to evaluate the performance of machine learning models, including LSTM networks, particularly in regression tasks such as predicting flow curves in material science. MSE measures the average squared difference

between the predicted values and the actual observed values in the dataset, with the formula:

$$MSE = \frac{1}{n} \sum_{i=1}^n (y_i - \hat{y}_i)^2 \quad (2-24)$$

Where:

- $\hat{y}_1, \hat{y}_2, \dots, \hat{y}_n$ are predicted values
- y_1, y_2, \dots, y_n are true values
- n is the number of data points in the dataset.

The MSE clearly indicates how well the model predicts, with smaller values indicating better predictive accuracy. A high MSE shows that the model predictions deviate significantly from the actual values, which suggests the need for model improvement. For LSTM models, MSE is useful because it penalizes larger errors more than smaller ones due to the squaring of the residuals. This helps capture the model to make precise predictions, especially in non-linear material deformation processes. In applications, such as predicting stress-strain relationships or flow curves in materials, MSE helps assess how closely the predictions align with experimental data and adjust model parameters or architecture to improve performance.

Furthermore, MSE is particularly useful with small datasets, which is often the case in material science research due to the high costs and time requirements of experimental data collection. In such cases, MSE allows the LSTM model to effectively adjust its internal parameters, including the weights of the hidden layers, to reduce prediction errors even with limited data. However, the quality of the dataset is important in determining MSE. If the data is noisy, incomplete, or not representative of the full range of conditions, the MSE may be artificially inflated and result in poor model generalization.

In summary, MSE is a powerful and widely applicable metric for evaluating the performance of LSTM networks in predicting material behavior, since it highlights both the magnitude and the frequency of errors in the predictions. By minimizing MSE, researchers can improve the accuracy of LSTM models and make more reliable predictions in domains, such as material science, where accurate forecasting of properties is critical for designing materials and optimizing manufacturing processes.

3. Methodology

3.1. Constitutive model

3.1.1. Flow curve fitting with Swift – Voce equation

For low strain-rate, we fit the stress-strain data with Swift – Voce equation. For high strain-rate, we fit the stress-strain data separately for high strain ($\varepsilon \geq 0.02$) and low strain with the modified Swift – Voce equation. The fitted parameters are then used to generate additional data for high strain values that are not available with experiment. The results at RT are shown in Table 3-1.

Table 3-1: Flow curve fitting results at RT.

Swift - Voce result:

| Condition | α | A | ε_0 | n | k_0 | Q | β_0 |
|----------------------------------|----------|-----------|-----------------|---------|-----------|-----------|------------|
| $\dot{\varepsilon} = 0.0001, RD$ | -0.0843 | 1855.4915 | 0.0005 | -0.2100 | 699.9021 | 528.6419 | 12990.0817 |
| $\dot{\varepsilon} = 0.0001, DD$ | -0.0351 | 1449.0665 | 0.0007 | -0.3575 | 654.2613 | 482.9348 | 11932.3490 |
| $\dot{\varepsilon} = 0.0001, TD$ | -0.0162 | 1859.3901 | 0 | -0.4505 | 670.9988 | 480.5649 | 11558.5423 |
| $\dot{\varepsilon} = 0.001, RD$ | -0.1499 | 829.4386 | 0 | -0.2021 | 1059.8279 | 54.5216 | 76.6431 |
| $\dot{\varepsilon} = 0.001, DD$ | -0.1696 | 896.9352 | 0 | -0.1862 | 1054.5637 | 61.0253 | 156.4644 |
| $\dot{\varepsilon} = 0.001, TD$ | -0.1573 | 898.7127 | 0 | -0.2040 | 1053.6354 | 92.6702 | 201.5890 |
| $\dot{\varepsilon} = 0.01, RD$ | -0.0412 | 1528.7965 | 0.0017 | -0.3426 | 538.6508 | 652.1925 | 6113.3657 |
| $\dot{\varepsilon} = 0.01, DD$ | -0.1439 | 786.6893 | 0.0000 | -0.2221 | 1062.3852 | 46.3042 | 130.3721 |
| $\dot{\varepsilon} = 0.01, TD$ | -0.0142 | 1595.8106 | 0.0013 | -0.4994 | 620.4402 | 543.5982 | 5095.2831 |
| $\dot{\varepsilon} = 0.1, RD$ | -0.1833 | 1344.1183 | 0.0001 | -0.1469 | 799.7405 | 427.7758 | 12388.0087 |
| $\dot{\varepsilon} = 0.1, DD$ | -0.2393 | 1821.1632 | 0 | -0.0894 | 1192.5889 | 128.4945 | 718.7260 |
| $\dot{\varepsilon} = 0.1, TD$ | 0.8197 | 1290.7194 | 0 | 0.0709 | -60.3743 | 1426.2732 | 638.7484 |

Modified Swift – Voce result:

| Condition | A | B | n | Q | ε_0 | α | β |
|--|-----------|---------|--------|-----------|-----------------|----------|---------|
| $\dot{\varepsilon} = 1, RD, \varepsilon < 0.02$ | 1581.8136 | 18.7997 | 0.1114 | 1891.1069 | 0.0031 | 0 | 19.9786 |
| $\dot{\varepsilon} = 1, RD, \varepsilon \geq 0.02$ | 1194.0092 | 14.7818 | 0.0373 | 759.6380 | 0 | 0 | 6.3350 |

3.1.2. Temperature dependency function parameter calibration

This section discusses the process of developing the temperature dependency function. It begins by studying the general trends in material behavior, followed by the

Methodology

selection of a suitable reference stress for normalization. The subsequent steps involve the development of temperature and strain-rate functions, and the calibration of each parameter within these functions. To validate the accuracy, fitting validation is conducted, and finally, simulation validation is performed.

3.1.2.1. *Material behavior analysis*

The data used for this analysis includes experimental data and extrapolated data obtained from Section 3.1.1 with strain values ranging from 0 to 3. The temperatures considered in the study range from 77.15 K to 673.15 K, while the strain-rates vary from 0.0001 to 0.1 as summarized in Table 3-2. As shown in the Figure 3-1, the material behavior demonstrates significant changes under these different loading conditions due to thermal softening, dynamic strain aging and adiabatic heating. Thermal softening refers to the decrease in material strength as temperature increases, due to increased atomic vibrations and weakening of atomic bonds. Dynamic strain aging occurs when solute atoms in the material interact with moving dislocations, causing fluctuations in the flow stress. Adiabatic heating is the increase in temperature caused by the rapid deformation of the material, leading to further changes in its mechanical properties.

Table 3-2: Data for temperature calibration.

| Tmp/StrRt | 77.15K | 233.15K | 298.15K | 373.15K | 473.15K | 573.15K | 673.15K |
|-----------|--------|---------|---------|---------|---------|---------|---------|
| 0.0001 | x | x | x | | | | |
| 0.001 | x | x | x | x | x | x | x |
| 0.01 | x | x | x | x | x | x | x |
| 0.1 | x | x | x | x | x | x | x |

3.1.2.2. *Reference stress*

After understanding the general trends, the next step is the selection of a suitable reference stress for normalization. Two options are considered: the yield strength at room temperature (RT) under quasi-static (QS) conditions, and the flow stress under the same conditions. It is determined that using the flow stress as the reference is more effective, as the use of a fixed yield stress for normalization results in scaled stress curves maintaining the same shape as the original curves.

$$f(T) = \frac{\sigma_T}{\sigma_{RT,QS}} \quad (3-1)$$

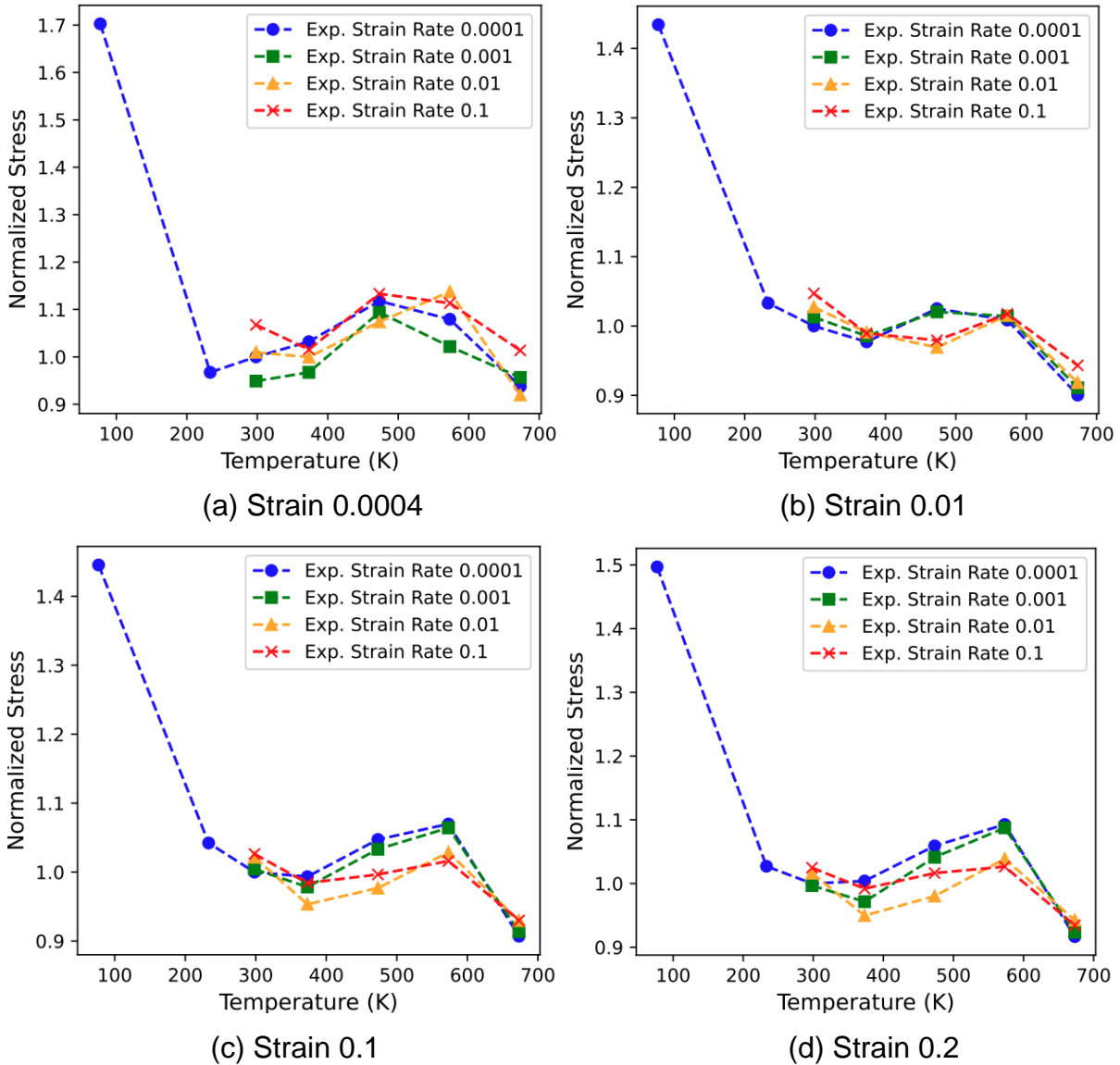


Figure 3-1. The distribution of the normalized stress over temperature at different plastic strain levels at rolling direction

3.1.2.3. Temperature dependency function

The modeling approach involves developing two equations to represent the temperature dependence of the material's stress response:

- Temperature function ($f(T, \varepsilon)$): This equation captures the thermal softening and dynamic strain aging effects on the material behavior.
- Thermal parameter function (C_i): This equation calibrates the thermal parameters used in the temperature function to achieve a comprehensive model applicable across different strain levels.

Existing literatures are explored, and various proposed functions are tested to understand their strengths and limitations. It is observed that some functions from the literature were oversimplified and unable to fully capture the trend, particularly at initial strains where the material undergoes elastic deformation. After numerous trials, the six-parameter function proposed by Shen (hereafter referred to as Shen's six-parameter equation) is identified as the most promising. This function consists of two key components: an exponential decay function to capture the effects of thermal softening, and an additional Gaussian function to address dynamic strain aging.

$$f(T, \varepsilon) = \frac{\sigma_T}{\sigma_{RT.QS}} = C_1(\varepsilon) \cdot \exp(-C_2(\varepsilon) \cdot T) + C_3(\varepsilon) + C_4(\varepsilon) \cdot \exp\left[-\left(\frac{T - C_5(\varepsilon)}{C_6(\varepsilon)}\right)^2\right] \quad (3-2)$$

Where:

- C_{1-6} are material parameters needed to be calibrated.
- C_1 and C_2 are related to the thermal activation components.
- C_3 generally, describes the athermal contribution.
- C_4 and C_6 are related to the intensity of the DSA and C_5 describes the corresponding characteristic temperature with the most intensive DSA at a certain strain level and strain-rate.

However, some limitations are still observed, particularly when dealing with small strains, and the function's sensitivity to initial guesses. To address these limitations, a nine-parameter function is developed. This function incorporates two components to handle dynamic strain aging, resulting in a more complex but improves overall fitting across all strain levels and reduced dependence on the initial guess. The performance of the six-parameter and nine-parameter functions are evaluated and discussed in the Section 4.1.2.

$$f(T, \varepsilon) = \frac{\sigma_T}{\sigma_{RT.QS}} = C_1(\varepsilon) \cdot \exp(-C_2(\varepsilon) \cdot T) + C_3(\varepsilon) + C_4(\varepsilon) \cdot \exp\left[-\left(\frac{T - C_5(\varepsilon)}{C_6(\varepsilon)}\right)^2\right] + C_7(\varepsilon) \cdot \exp\left[-\left(\frac{T - C_8(\varepsilon)}{C_9(\varepsilon)}\right)^2\right] \quad (3-3)$$

Where:

- C_{1-9} are material parameters needed to be calibrated.

The next step is to calibrate the thermal parameters used in the temperature function $f(T, \varepsilon)$. The aim is to develop a single function that can represent all the parameters as a function of strain, rather than using individual calibrations for each parameter. This approach ensures a more comprehensive and consistent model that can be applied across different strain levels. The following function is proposed to calibrate as follows:

$$C_i = f(\varepsilon) = Q_1 \cdot \exp\left(-\frac{(\varepsilon - Q_2)^2}{2 \cdot Q_3^2}\right) + P_1 \cdot \exp(-P_2 \cdot \varepsilon) + M_1 \cdot \exp\left(-\frac{(\varepsilon - M_2)^2}{2 \cdot M_3^2}\right) + \frac{N_1}{1 + \exp(-N_2 \cdot (\varepsilon - M_2))} \quad (3-4)$$

Where:

- $Q_{1\sim 3}$, $P_{1\sim 2}$, $M_{1\sim 3}$, and $N_{1\sim 2}$ are parameters needed to be calibrated.

The parameters C_i are not constants. They vary with strain to capture the complex material behavior, such as rapid changes at low strain, peaks at intermediate strain, and stabilization at higher strain values. The first Gaussian in the Equation (3-4) effectively models initial peak or rise that exhibit at very low strains. The exponential decay quickly reduces the effect after the initial peak, which is useful for fitting datasets with an immediate drop after a rise. The second Gaussian allows the function to capture intermediate peaks that occur as the strain continues to increase. The logistic function ensures that the curve stabilizes as strain increases, which is common in material response where properties reach a plateau at high levels of deformation. The graphs of these parameters are presented in Section 4.1.2.

3.3.2.4. Validation

In the final step, the results of the two fitting equations are combined to validate the stress predictions. The C_i parameter values obtained from the thermal parameter calibration are plugged into the temperature function $f(T, \varepsilon)$ to derive the stress values. These fitting results are compared with the experimental and extrapolated data to validate the accuracy of the model.

3.1.3. Strain-rate dependency function parameter calibration

This chapter discusses the process of parameter calibration for strain-rate dependency. This process contains three steps: Analyzing the relationship between stress, strain and strain-rate with experimental data, finding strain-rate dependent function and calibrating the function's parameters.

3.1.3.1. *Experimental data*

For strain-rate dependency, the data used for calibration is strictly derived from experimental results at low strain ($\varepsilon < 0.08$). At higher strain levels, it is difficult to isolate strain-rate effects from other phenomena such as strain hardening, localized deformation, or material instability. As the material behavior is no longer solely dominated by strain-rate sensitivity, the calibration is less reliable. In this study, the data consists of 5 temperatures at rolling direction as shown in Table 3-3.

Table 3-3: Data for strain-rate calibration.

| Tmp/StrRt | 298.15K | 373.15K | 473.15K | 573.15K | 673.15K |
|-----------|---------|---------|---------|---------|---------|
| 0.0001 | x | x | x | x | x |
| 0.001 | x | x | x | x | x |
| 0.01 | x | x | x | x | x |
| 0.1 | x | x | x | x | x |
| 1 | x | | | | |

For calibration, the stress is normalized with the reference stress described in equation (3-1). From the strain-rate dependent flow curve in Figure 3-2 and normalized stress in Figure 3-1, the stress values at different strain-rate varies as temperature increase. For example, at 573.15K, the stress value is higher at lower strain-rate whereas at 673.15K, the stress value decreases as strain-rate increases. Overall, as temperature increases, the strain-rate sensitivity becomes more prominent. This could be due to thermally activated mechanisms that enhance the material's sensitivity to deformation rate.

Methodology

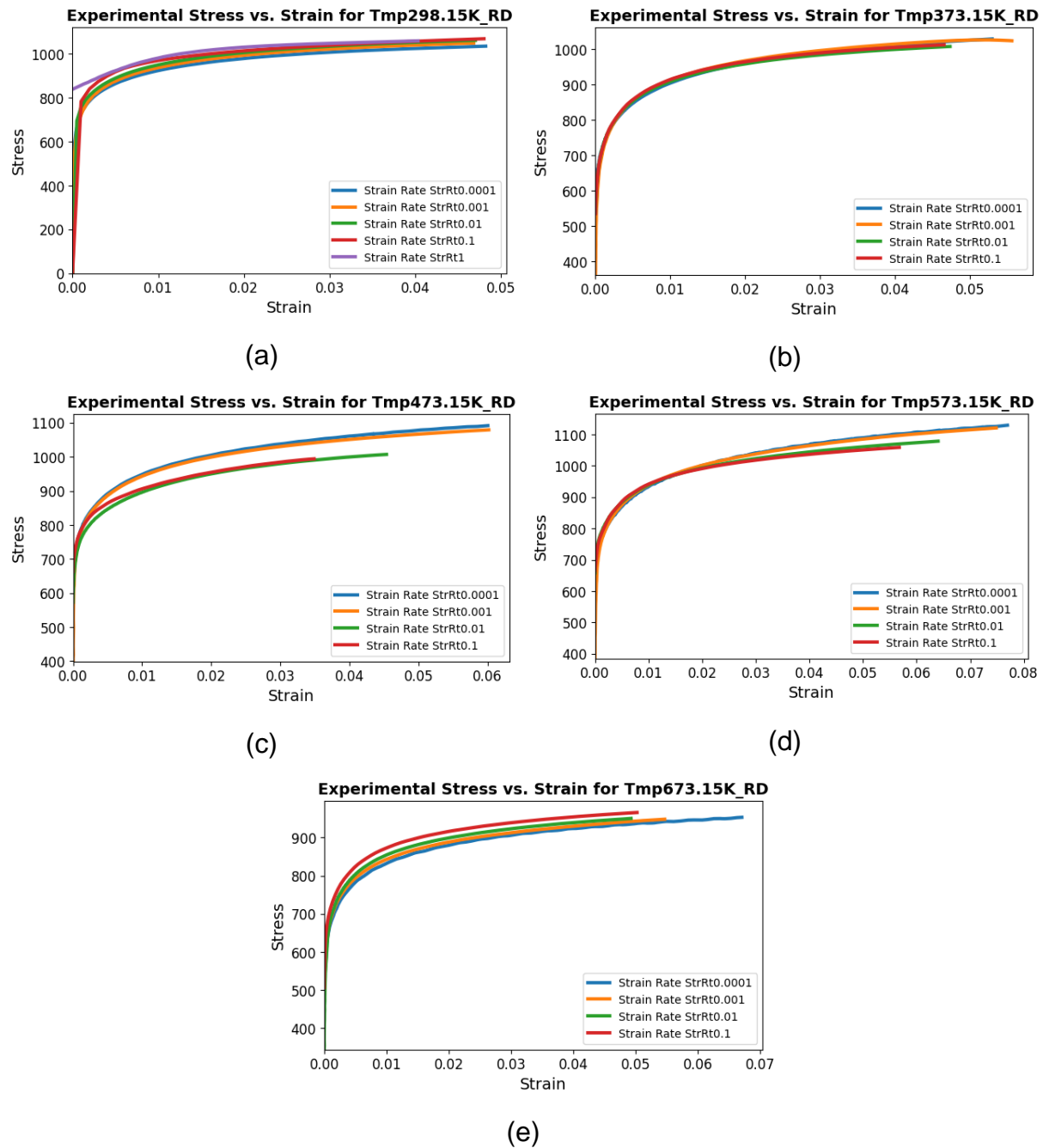


Figure 3-2: Strain-rate dependency for 298.15K, 373.15K, 473.15K, 573.15K, 673.15K at rolling direction (RD).

3.1.3.2. Strain-rate dependency function

This section explores different functions used for strain-rate dependency, including a new proposed function and existing functions from literature (Power law model, Wagoner model, other student's proposal). Generally, the behaviors of strain-rate dependency are non-linear and fluctuated across different temperatures. To represent this relationship, the function should be able to capture inflection points and curvature.

Methodology

The Power-law model and the Wagoner model are described in Equation (3-5) and Equation (3-6) respectively. These equations, however, do not perform well for DP1000 experimental data. They assume that the relationship between the normalized stress and strain are of simple mathematical forms (power-law and square-root terms) and lack terms like quadratic or logarithmic contributions. Similar to the Power-law model and the Wagoner model, other students' proposal, as described in Equation (3-7), assumes that the normalized stress-strain relationship is nearly linear or simple logarithmic function. For this experimental data, there are deviations and bending patterns that cannot be captured by a linear-log model.

$$f(\dot{\varepsilon}) = \frac{\sigma_{\dot{\varepsilon}}}{\sigma_{\text{ref}}} = \left(\frac{\dot{\varepsilon}}{\dot{\varepsilon}_{\text{ref}}} \right)^m \quad (3-5)$$

$$f(\dot{\varepsilon}) = \frac{\sigma_{\dot{\varepsilon}}}{\sigma_{\text{ref}}} = \left(\frac{\dot{\varepsilon}}{\dot{\varepsilon}_{\text{ref}}} \right)^{m_0} \sqrt{\dot{\varepsilon} \cdot \dot{\varepsilon}_0^{\frac{m_1}{m_0}}} \quad (3-6)$$

$$f(\dot{\varepsilon}) = \frac{\sigma_{\dot{\varepsilon}}}{\sigma_{\text{ref}}} = (C_1 \cdot \ln(\dot{\varepsilon}) + C_2) \quad (3-7)$$

To capture the complex behavior of strain-rate dependent stress, we proposed a new equation, adapted from Equation (3-7). This new equation, shown in Equation (3-8), has two additional terms C_3 and C_4 .

$$f(\dot{\varepsilon}) = \frac{\sigma_{\dot{\varepsilon}}}{\sigma_{\text{ref}}} = C_1 \ln(\dot{\varepsilon}) + C_2 \cdot \dot{\varepsilon}^{C_3} + C_4 \cdot (\ln(\dot{\varepsilon}))^2 \quad (3-8)$$

Where:

- C_1 : This parameter captures the linear relationship between the normalized stress and the natural logarithm of the strain-rate $\ln(\dot{\varepsilon})$. It represents the primary linear trend in the data and is crucial for modeling the direct proportionality between stress and strain-rate in logarithmic space.
- C_2 : This parameter is associated with a nonlinear term involving the strain-rate raised to the power C_3 . It captures deviations from the linear trend introduced by C_1 , accounting for the strain-rate-sensitive behavior that may not align with simple logarithmic scaling.
- C_3 : This exponent controls the power-law scaling of the strain-rate. It determines how sensitive the stress response is to changes in the strain-rate in the nonlinear term. Together with C_2 , it enables the model to fit more complex curvature or slope changes in the data.

Methodology

- C_4 : This parameter quantifies the contribution of the quadratic term involving $(\ln(\varepsilon))^2$. It helps capture higher-order effects, such as curvature or deviations in the data that cannot be explained by the linear or the nonlinear terms. This term ensures the flexibility of the model to account for more detailed patterns in the stress-strain-rate relationship.

In summary, C_1 provides the primary linear scaling. C_2 and C_3 enable nonlinear adjustments. C_4 captures higher-order effects for improved accuracy.

3.1.3.3. Strain-rate parameters calibration

This project experiments two methods of parameters calibration: Fixed parameters and parameters evolving with strain. For the first method, the fixed parameters are chosen as the average of C_i at all strain. However, this approach has a major flaw. The fixed parameters for all strain result in stress at different strain is the same and no evolving, as seen in Figure 3-3.

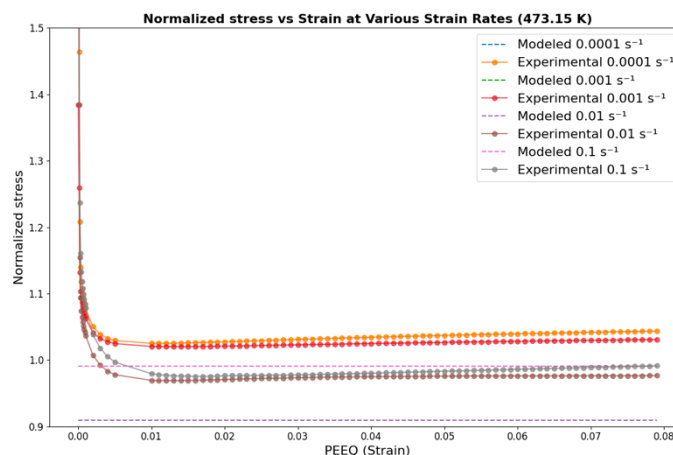


Figure 3-3: Normalized stress vs PEEQ for fixed strain-rate parameters.

The second method, parameters evolving with strain, solves this challenge since strain-rate dependency changes as strain increases as seen in Figure 3-4. To reflect this phenomenon, each parameter is calibrated within low strain, intermediate strain and high strain according to the material behaviors. That is, for each parameter, three equations are suggested. At low strain or elastic region, DP1000 exhibits a steep elastic response due to the martensitic phase, which is stiff and resists deformation. After the yielding point, the material transitions into plastic deformation, where the ferritic phase starts to deform, contributing to the ductility of the material. As strain

Methodology

increases, work hardening dominates due to the interaction between ferritic and martensitic phases, resulting in a non-linear stress-strain response.

The optimal thresholds are at strain 0.002 and 0.04 respectively. The value 0.002 is an important threshold because it marks the transition from the elastic to the early plastic deformation region, where material behavior starts to deviate from linearity. Similarly, the value 0.04 is chosen by trials and errors. This value represents the onset of significant strain hardening, where the material's resistance to deformation increases substantially. The equations for C_i are shown below.

$$C_1 = \begin{cases} a_1 e^{b_1 \varepsilon} + c_1 + d_1 \varepsilon^2 + e_1 \varepsilon, & \varepsilon < 0.002 \\ a_2 \sin(b_2 \varepsilon + c_2) e^{-d_2 \varepsilon} + e_2 \varepsilon^2 + f_2 \varepsilon + g_2, & 0.002 < \varepsilon < 0.04 \\ a_3 e^{b_3 \varepsilon} + c_3 & \varepsilon > 0.04 \end{cases} \quad (3-9)$$

- Low strain: The exponential term $a_1 e^{b_1 \varepsilon}$ captures rapid changes in stress associated with elastic deformation. Polynomial terms refine the curve to account for small variations in stress at very low strains.
- Intermediate strain: The damped sinusoidal term describes oscillatory stress behavior due to microstructural changes during elastic-plastic transition.
- High strain: Exponential growth represents work hardening in the plastic regime, where stress increases steadily.

$$C_2 = \begin{cases} a_1 \ln(\varepsilon) + b_1 \varepsilon^{c_1} + d_1 e^{-\varepsilon}, & \varepsilon < 0.002 \\ a_2 \ln(\varepsilon) + b_2 \varepsilon^{c_2} + d_2 e^{-\varepsilon}, & 0.002 < \varepsilon < 0.04 \\ a_3 \ln(\varepsilon) + b_3 \varepsilon^{c_3} + d_3 e^{-\varepsilon} & \varepsilon > 0.04 \end{cases} \quad (3-10)$$

- Low strain: Logarithmic term $\ln(\varepsilon)$ captures rapid stress changes at very small strains. Power-law term ε^{c_1} models nonlinear trends, while $e^{-\varepsilon}$ adjusts for diminishing contributions.
- Intermediate strain: Similar terms as above, adjusted for the intermediate strain range to account for material-specific trends during elastic-plastic transition.
- High strain: Logarithmic and power-law terms dominate, capturing gradual stress increases during plastic deformation.

$$C_3 = \begin{cases} a_1 \varepsilon^3 + b_1 \varepsilon^2 + c_1 \varepsilon + d_1, & \varepsilon < 0.002 \\ a_2 \varepsilon^3 + b_2 \varepsilon^2 + c_2 \varepsilon + d_2, & 0.002 < \varepsilon < 0.04 \\ a_3 \varepsilon^2 + b_3 \varepsilon + c_3 & \varepsilon > 0.04 \end{cases} \quad (3-11)$$

Methodology

- Low strain: Cubic polynomial provides flexibility to fit nonlinear elastic behavior at small strains.
- Intermediate strain: Cubic terms continue to describe the nonlinear transition into plastic deformation.
- High strain: Quadratic form is sufficient to model stable stress evolution during plastic deformation.

$$C_4 = \begin{cases} a_1 e^{b_1 \cdot \varepsilon} \cos(c_1 \varepsilon) + d_1 & \varepsilon < 0.002 \\ a_2 \sin(b_2 \varepsilon + c_2) e^{\{-d_2 \varepsilon\}} + e_2 \varepsilon^2 + f_2 \varepsilon + g_2, & 0.002 < \varepsilon < 0.04 \\ a_3 e^{b_3 \varepsilon} + c_3 & \varepsilon > 0.04 \end{cases} \quad (3-12)$$

- Low strain: The exponential term captures rapid stress changes, while the cosine term accounts for potential oscillations in stress at very low strains.
- Intermediate strain: The damped sinusoidal term describes microstructural effects, with polynomial terms handling broader trends.
- High strain: Exponential growth captures the strain-hardening behavior at high strains.

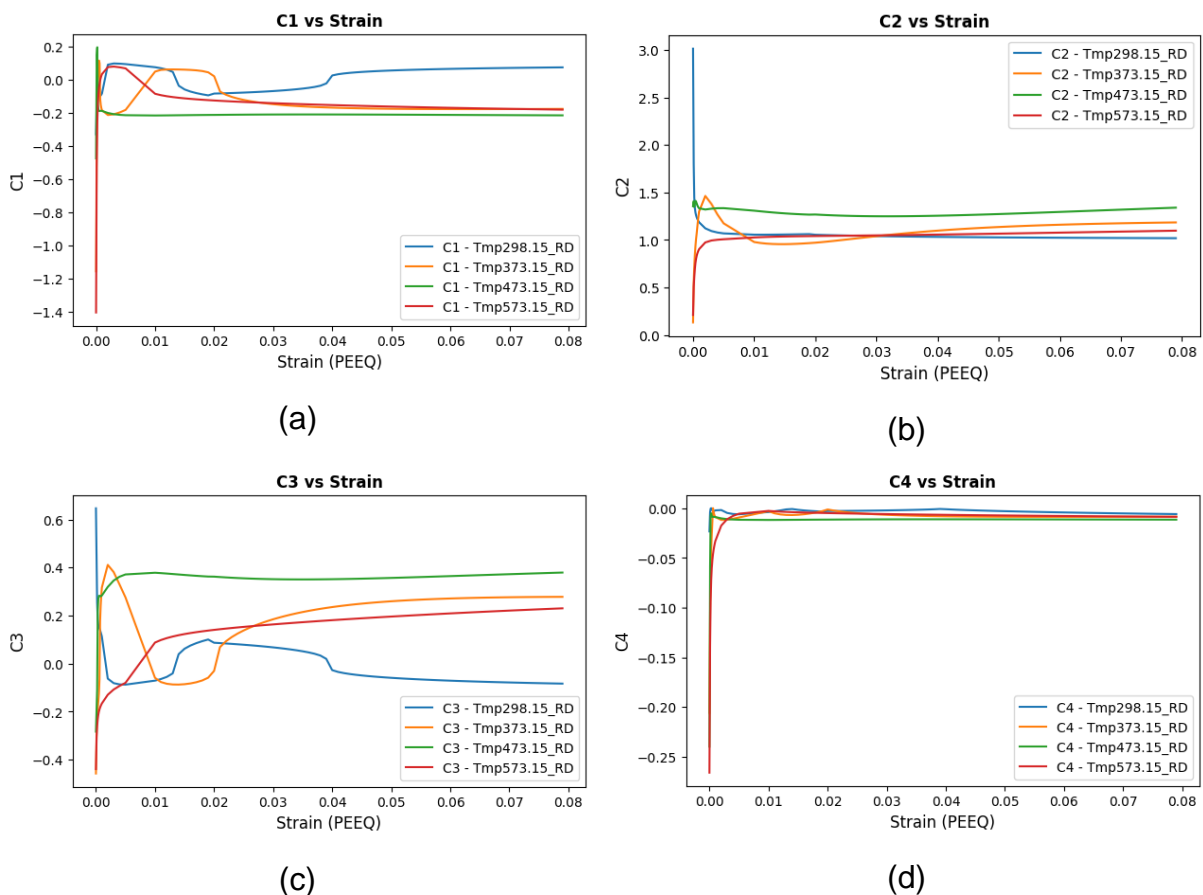


Figure 3-4: Strain-rate dependent parameters evolving with strain

3.2. Machine Learning-based model: Long Short-Term Memory

The development of a machine learning model to predict stress-strain behavior is centered around a Long Short-Term Memory (LSTM) neural network, chosen for its ability to model sequential data effectively. Stress-strain relationships evolve as strain increases, and LSTM models are uniquely suited to capture such long-term dependencies. The proposed model utilized plastic strain, temperature, and strain-rate as inputs to predict normalized stress, ensuring that it could capture the coupled effects of temperature and strain-rate on material behavior. The workflow included systematic data preparation, model architecture design, and iterative evaluation to achieve optimal performance.

3.2.1. Data preprocessing

Data preparation began with collecting experimental flow curves obtained in the rolling direction (RD). These curves span a temperature range of 298.15 K to 673.15 K and strain-rates from 0.0001 to 0.1, resulting in a dataset of 20 flow curves. We plot the available data as shown in Appendix Fig.1. The dataset was preprocessed to ensure consistency and suitability for the model. Normalization is applied to all inputs and outputs, scaling plastic strain, temperature, strain-rate, and normalized stress to a uniform range. This step was essential to stabilize training and allow the model to converge efficiently. The dataset was then split into training and testing subsets. The training set consisted of a varying number of flow curves—ranging from 8 to 19 FCs—to analyze the impact of dataset size on the performance of LSTM model, while the testing set is used to evaluate the generalization of the model.

3.2.2. Model Architecture and Implementation

The architecture of the LSTM model was carefully designed to handle the complexity of the problem. The input layer accepted three features—plastic strain, temperature, and strain-rate—and passed them through three hidden layers with 150, 370, and 370 neurons, respectively. These layers provided the model with sufficient capacity to learn complex patterns without becoming computationally prohibitive. The output layer consisted of a single neuron that predicted normalized stress. The model used the Rectified Linear Unit (ReLU) activation function to introduce nonlinearity in the hidden layers, while the Adam optimizer was employed to efficiently adjust weights during training. The mean squared error (MSE) is chosen as the loss function to minimize the

Methodology

difference between the predicted and actual normalized stress values. Training was conducted over 50 epochs with a batch size of 32, balancing training efficiency and model stability given the relatively small dataset size.

The development and evaluation of the LSTM model followed an iterative workflow. Initially, the model was trained using a subset of flow curves, starting with 8 FCs. The trained model was then evaluated on the testing set using R^2 (coefficient of determination) and MSE as performance metrics. Based on these results, adjustments were made to the model's hyperparameters, including the number of neurons and learning rate, to improve performance. This process was repeated with progressively larger training datasets, such as 12, 15, 16, and 19 FCs, to identify the optimal training set size for balancing accuracy and generalization.

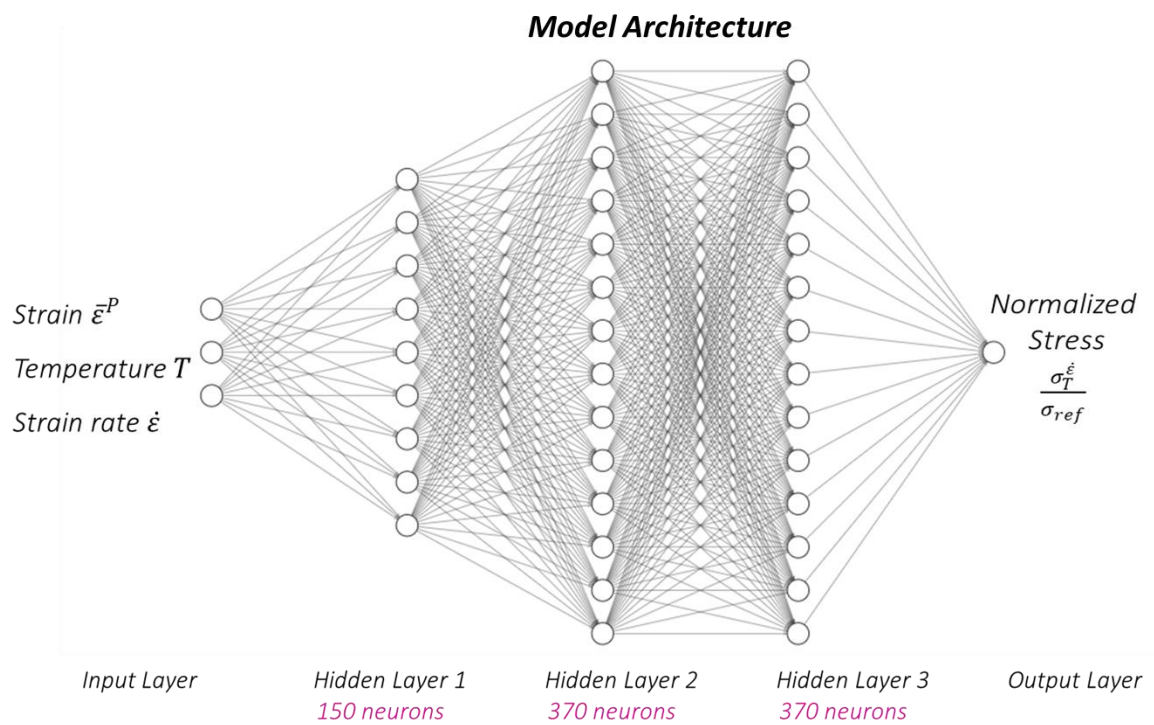


Figure 3-5: Visualization of LSTM Model Architecture.

3.3. Validation

This section introduces procedures that will be used to validate both the constitutive and the machine learning models introduced earlier. This validation stage is highly crucial as it evaluates the models' effectiveness when applied in actual cases.

A critical application that is used throughout the study is Abaqus. This software is a simulation platform that is used in engineering and research for FEM analysis. This study uses Abaqus to generate force-displacement data for the material. The simulation is conducted by incorporating stress-strain flow curves along the RD, DD, and TD directions and their respective r-values, which can be obtained during the process discussed in Section 3.1.1, into a material file. This file is then provided to the system along with the enHill48-incorporated-VUMAT subroutine and the job inputs for five different geometries: CH6hw, NDBR6, NDBR20r, NDBR50f, and shear specimen (SH) for the simulation to begin. However, this study's simulations are too complex to be conducted on personal computers. For that reason, access tokens to the Puhti supercomputer are granted so that the simulations can be executed with the help of advanced hardware. Still, a job batch would take around 30 to 50 hours to complete. Yet, the output database (ODB) files yielded after each job cannot be used immediately. To counter the problem, the files are processed using the Abaqus CAE graphical user interface to extract force-displacement data as text (.txt) files.

The validation phase incorporates two different approaches for both of our models. First, the LSTM machine learning model was utilized to generate stress-strain data for strain-rate 0.0001 s^{-1} and temperature 773.15K (equivalent to 500 degrees Celsius). This condition was chosen because it had yet to be included in the original datasets used to train the LSTM model. Therefore, this is an excellent opportunity to assess the model's performance on unfamiliar data. The generated data was used to run the Abaqus simulation to obtain the respective force-displacement data, which was then graphed along with the experimental force-displacement data for accuracy evaluation. In our constitutive model, we want to validate the model by assessing the capability of both models separately and evaluating their ability as a joint model. In the former method, flow curves are generated using the calibrated temperature and strain-rate functions developed earlier, which are then serve as inputs for Abaqus simulations, as detailed earlier in this paper. The result of this method will be presented later in this paper.

Methodology

In the second approach, we aim to represent correctly the interaction of the temperature effects with the influence of strain-rate on material behavior under dynamic conditions. For capturing this, we introduce a unified function, $f(T, \dot{\varepsilon}, \varepsilon)$ that includes both the temperature function, $f(T)$, and the strain-rate function, $f(\dot{\varepsilon})$, which is as follows:

$$f(T, \dot{\varepsilon}, \varepsilon) = K \cdot f(T) \cdot f(\dot{\varepsilon}) \quad (3-13)$$

A crucial component in our unified model is the constant K , which serves as the harmonizing effect of the $f(T)$ and $f(\dot{\varepsilon})$. For this purpose, the Taylor-Quinney coefficient beta is utilized. This choice is substantiated by the work of Liu et al., who demonstrated that β quantifies the fraction of plastic work converted into heat. This equation can be used to illustrate the effect of strain-rate in the rise of temperature; therefore, it is the ideal parameter to unite the two modules of temperature and strain-rate in this case.

We can calculate the value of β using an equation of strain-rate (Liu et al., 2020):

$$\beta = \frac{\beta_i}{2} \left\{ 1 + \tanh \left[S_c \cdot \log \left(\frac{\dot{\varepsilon}}{\dot{\varepsilon}_c} \right) \right] \right\} \quad (3-14)$$

Where:

- β is the desired Taylor-Quinney coefficient
- β_i is the value of Taylor-Quinney at very high strain-rates, where adiabatic conditions are assumed
- $S_c, \dot{\varepsilon}, \dot{\varepsilon}_c$ are specific heat fraction parameters
- $\dot{\varepsilon}$ represents the strain-rate

The value of $\beta_i, S_c, \dot{\varepsilon}_c$ are listed in Table 3-4, making it easy to calculate the value of β by just plugging in the strain-rate value. By doing so, this model is not only empirically based, but also enhances predictive accuracy by filling the gap in mechanical and thermal responses of material under dynamic loading.

Table 3-4: Calibrated specific heat fraction parameters of DP1000 in the eMBW model. (Liu et al., 2020)

| Notion | β_i | S_c | $\dot{\varepsilon}_c$ |
|--------|-----------|-------|----------------------------------|
| Value | 0.9 | 0.58 | $0.0043 \text{ (s}^{-1}\text{)}$ |

4. Results & Discussion

4.1. Constitutive model

4.1.1. Flow curve fitting with Swift – Voce equation

This section assesses how effectively the Swift-Voce equation fits the flow curves of DP1000 steel across various conditions. To conduct the analysis, we first generated material input files from the fitted flow curves, which were then used in Abaqus simulations as described in Section 3.3. The simulated force-displacement curves were compared to corresponding experimental data in order to evaluate the capability of the model. Altogether, around 305 Abaqus simulations were conducted in a wide range of conditions.

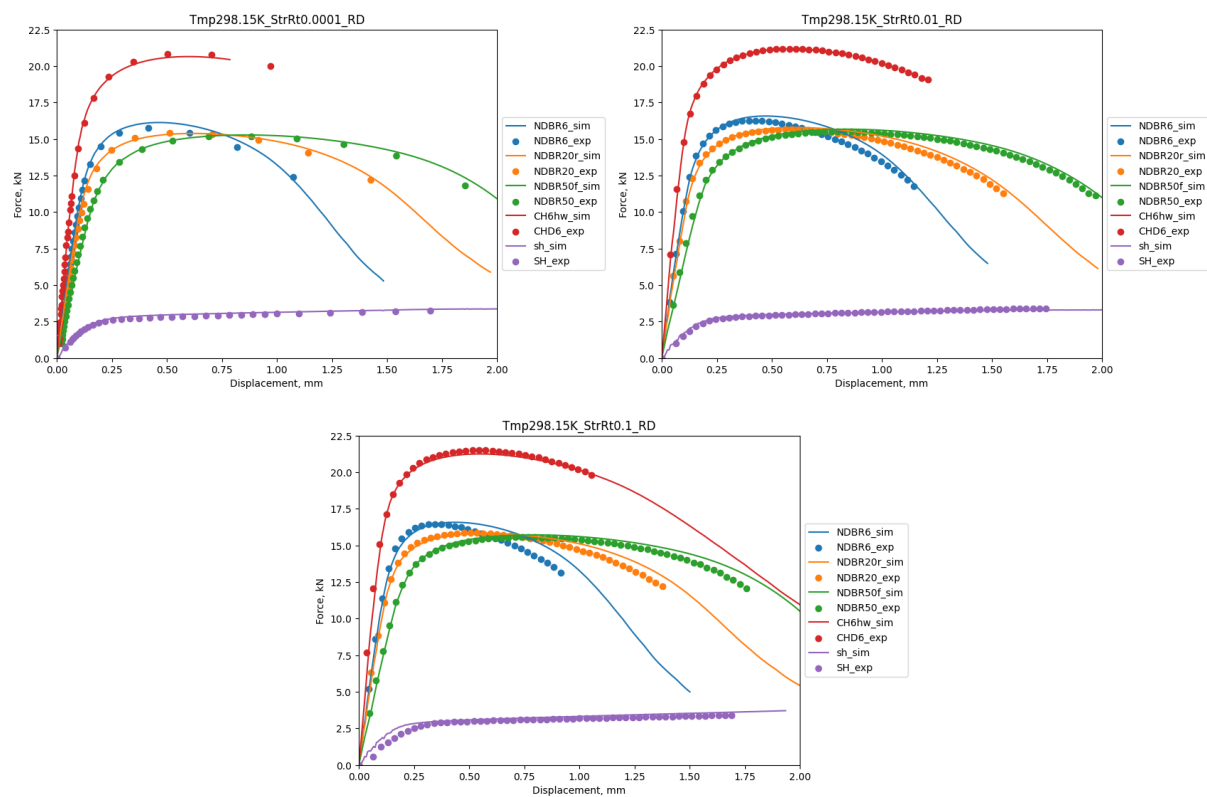


Figure 4-1: Force-displacement curves at Room Temperature for Strain-rate of: a) 0.0001, b) 0.01, c) 0.1.

Figure 4-1 displays the force-displacement curves at room temperature for the three different strain-rates. The graphs exhibit excellent fitting quality, with R^2 values exceeding 0.99 in all tested scenarios. For other conditions, while the fitting quality may not match this precision, the simulated data still effectively captures the general trends of the experimental curves.

Results & Discussion

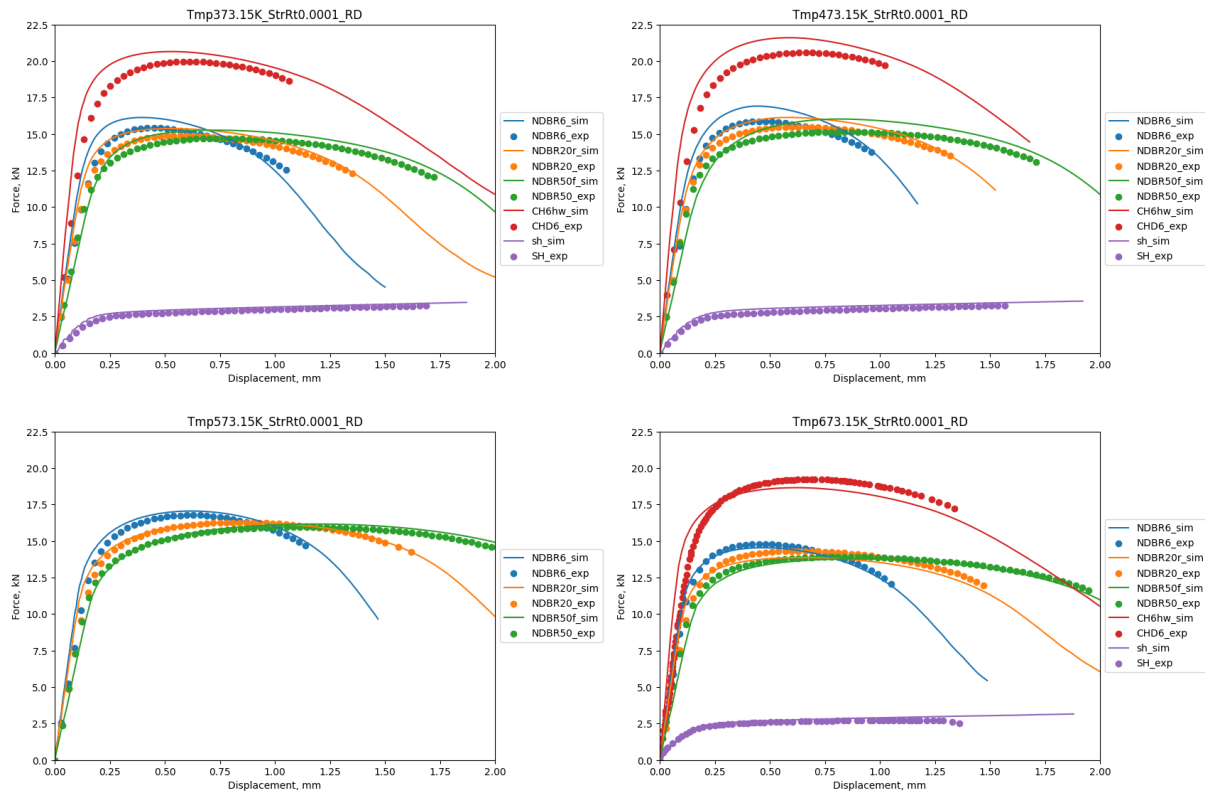


Figure 4-2: Force-displacement curves for quasi-static strain-rate at: a) 373.15K, b) 473.15K, c) 573.15K, d) 673.15K.

The Swift-Voce further highlighted the excellent capabilities in fitting data under varying temperature conditions, illustrated in Figure 4-2. At 373.15K and 473.15K, the simulations align closely with the experimental data, especially during the initial elastic-plastic transition and early displacement phase – though minor deviations were reflected at around the peak points.

At higher temperatures (573.15K), this model fits well with experimental curves for all geometries, both in peak force and post-peak behaviors. There is one minor problem with the results of 573.15K, though, is that data for only three geometries can be obtained from the simulation. Nonetheless, given the almost perfect fitting quality, the results still look promising.

At 673.15K, the fit is strong, although slight misalignments were noted for the CH6hw geometry, especially near peak displacement.

Regardless of these minor defects, the Swift-Voce model gives a admirable prediction in all temperatures conditions, but it shows almost perfect accuracy for room temperature. The model's ability to capture the material behavior under various conditions comfirms its suitability for modelling the DP1000 steel. Future work will be able to develop this model further, with improvements in performance on certain geometries and capabilities to operate on different datasets. Overall, the results are promising, and there is great potential for further advancements.

4.1.2. Temperature dependency function parameter calibration

4.1.2.1. *Shen's six-parameter equation*

As presented in Figure 4-3, Figure 4-4, Figure 4-5, and Figure 4-6, the six-parameter function shows a stable result across the complete temperature range and various strain values and strain-rates. It is able to capture the reduction in material strength from lower to intermediate temperatures (77.15 K to 233.15 K) as well as the gradual increase at higher temperatures (298.15 K to 573.15 K), followed by a decrease at very high temperatures (673.15 K). The shape of the curve remains stable across different strain values, indicating consistent material behavior.

Figure 3-4 shows that the six-parameter function achieves the best prediction accuracy at strain-rates of 0.001 and 0.01, with average R-squared values of 0.998 and 0.996, respectively. However, it is observed that the results are less stable at small strain values, such as 0.00011. This phenomenon occurs across all strain-rates tested. The reduced accuracy at small strain values can be attributed to the material's behavior in the elastic deformation region. During elastic deformation, the stress-strain relationship is linear, and the material's response is primarily governed by its elastic modulus, which is less sensitive to temperature and strain-rate variations compared to the yield and flow stresses. The six-parameter function, which is primarily designed to capture the thermal softening and dynamic strain aging effects on the flow stress, may not be as effective in modeling the elastic region of the stress-strain curve.

Results & Discussion

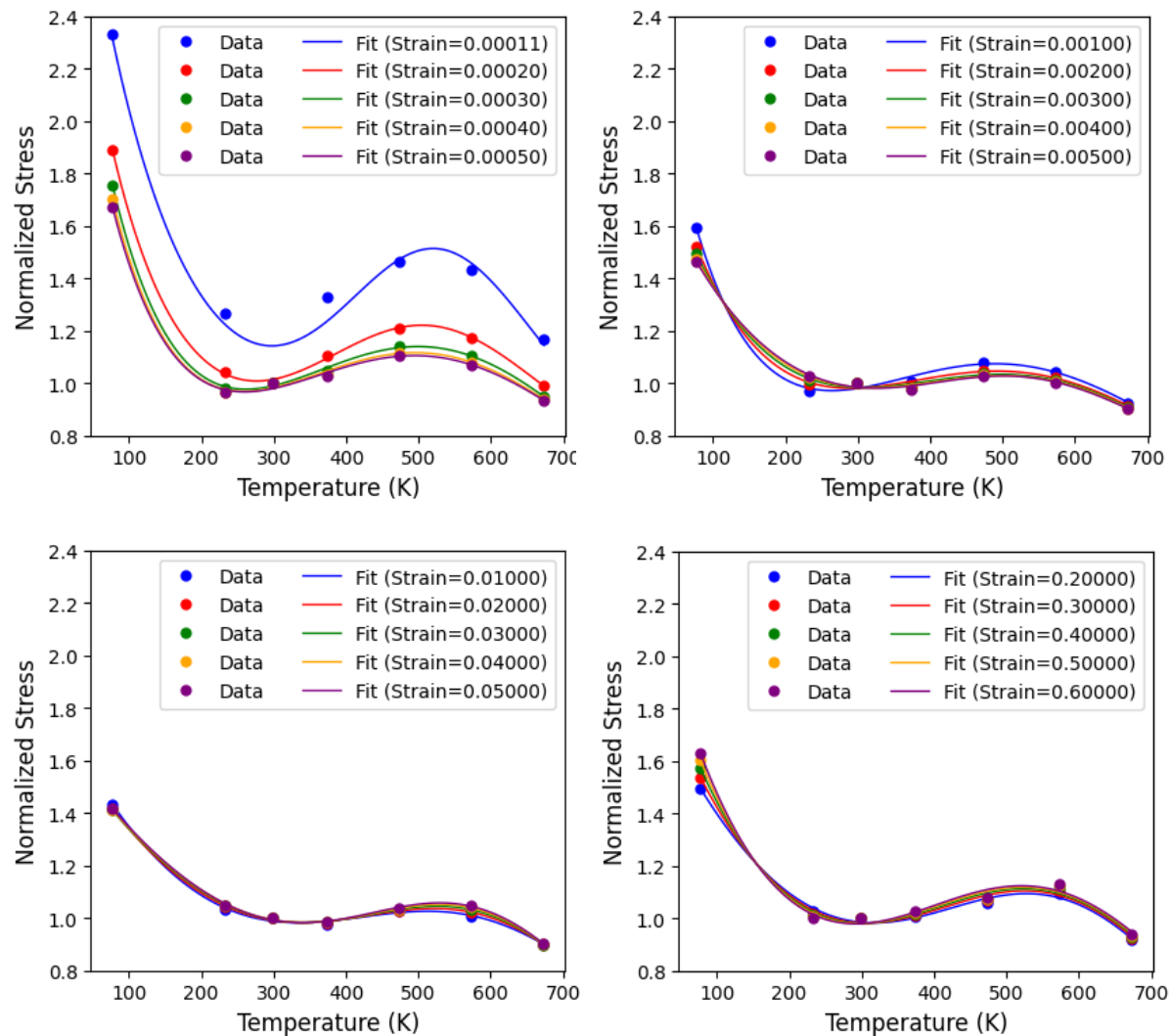


Figure 4-3. The prediction of six-parameter equation for the normalized stress in comparison with experimental and extrapolated data at strain-rate 0.0001 considering different plastic strain levels.

Results & Discussion

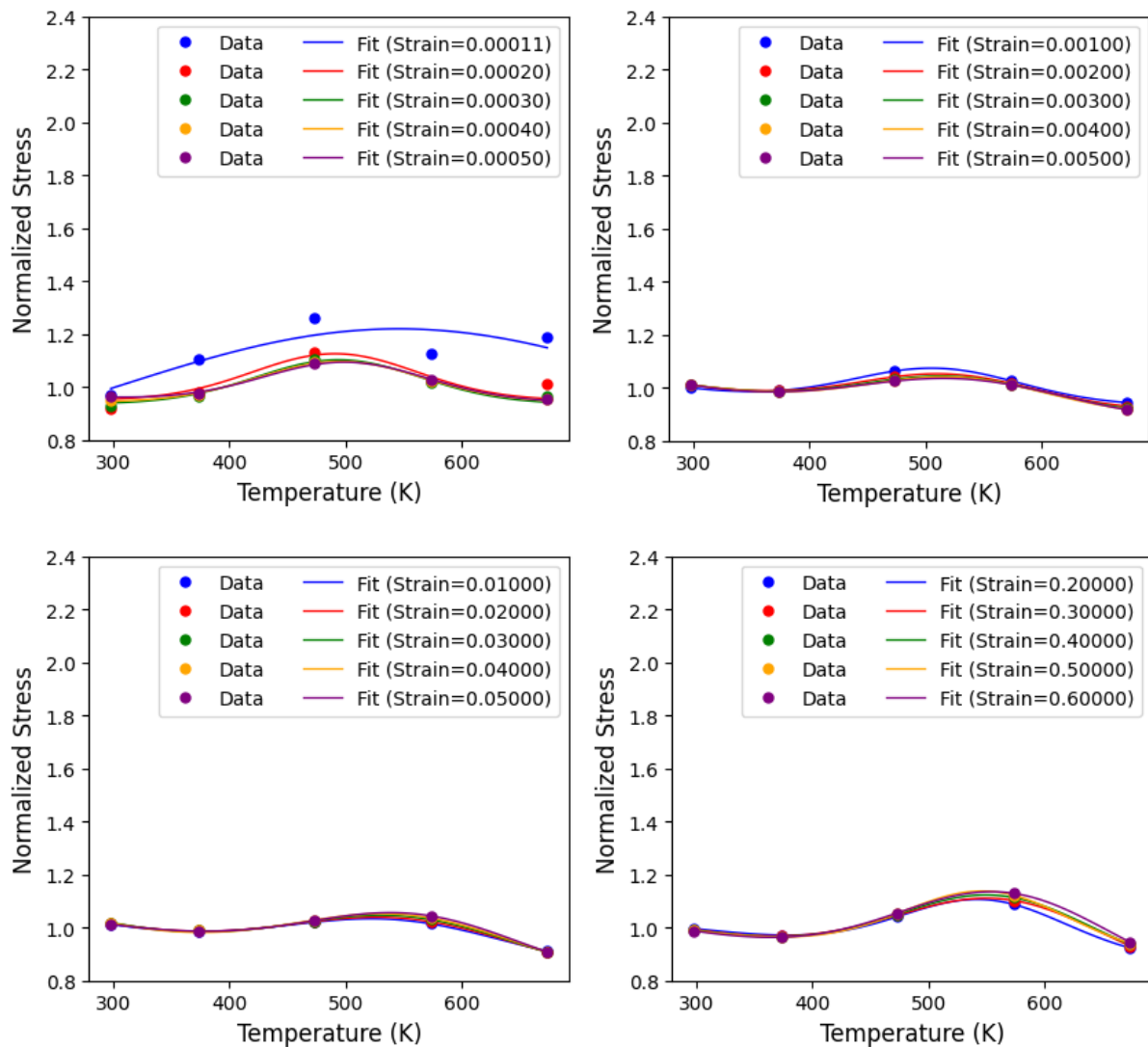


Figure 4-4. The prediction of six-parameter equation for the normalized stress in comparison with experimental and extrapolated data at strain-rate 0.001 considering different plastic strain levels.

Results & Discussion

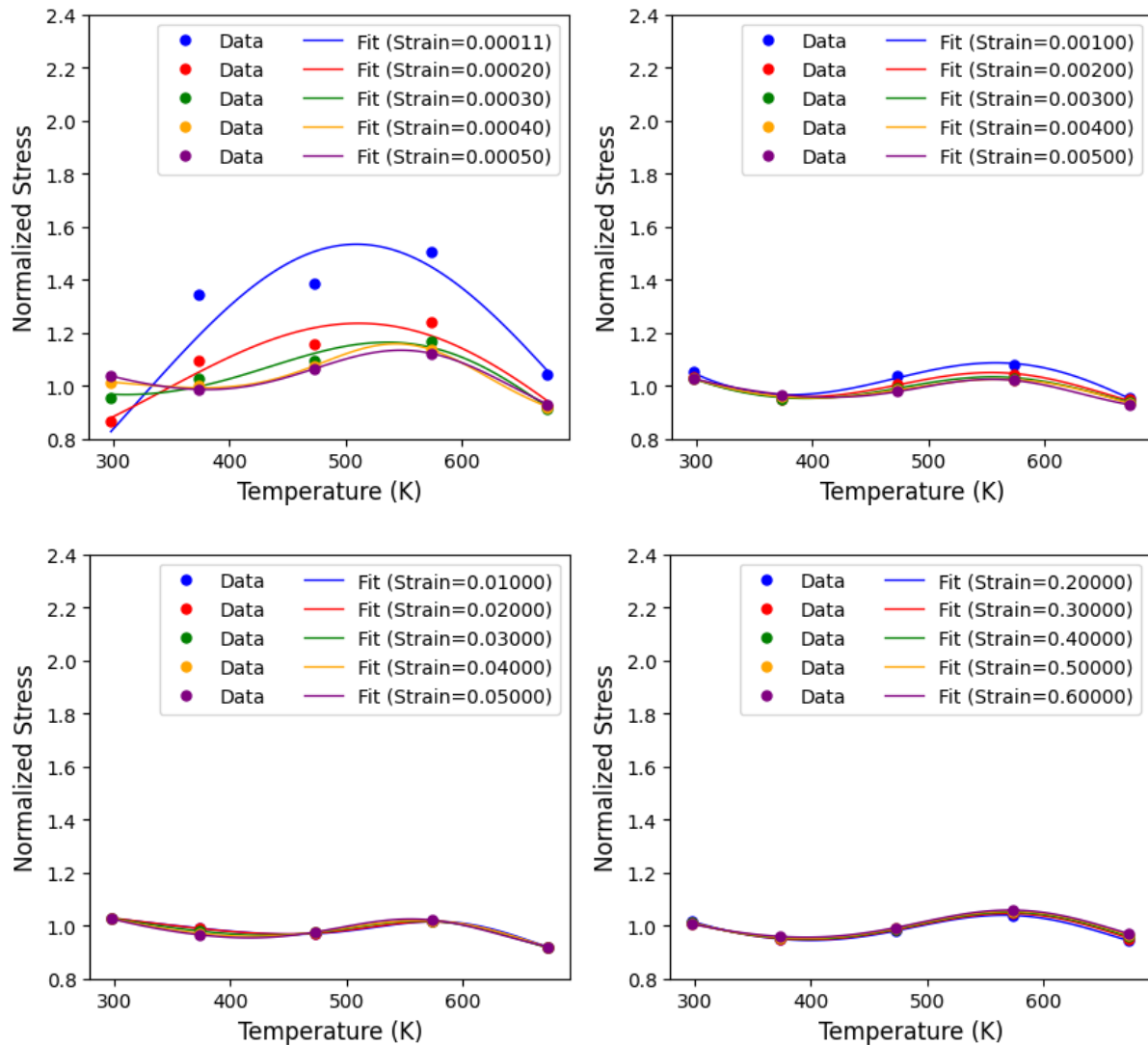


Figure 4-5. The prediction of six-parameter equation for the normalized stress in comparison with experimental and extrapolated data at strain-rate 0.01 considering different plastic strain levels.

Table 4-1: The r-squared value of prediction curves at different strain-rates of the six-parameter function.

| R-squared / Strain-rate | 0.0001 | 0.001 | 0.01 | 0.1 |
|-------------------------|--------|--------|--------|--------|
| Function | 0.971 | 0.685 | 0.87 | 0.449 |
| Smallest value | 1 | 1 | 1 | 1 |
| Largest value | 0.994 | 0.998 | 0.996 | 0.987 |
| Average value | 99.75% | 98.48% | 84.81% | 94.94% |
| R-squared | 0.971 | 0.685 | 0.87 | 0.449 |

Results & Discussion

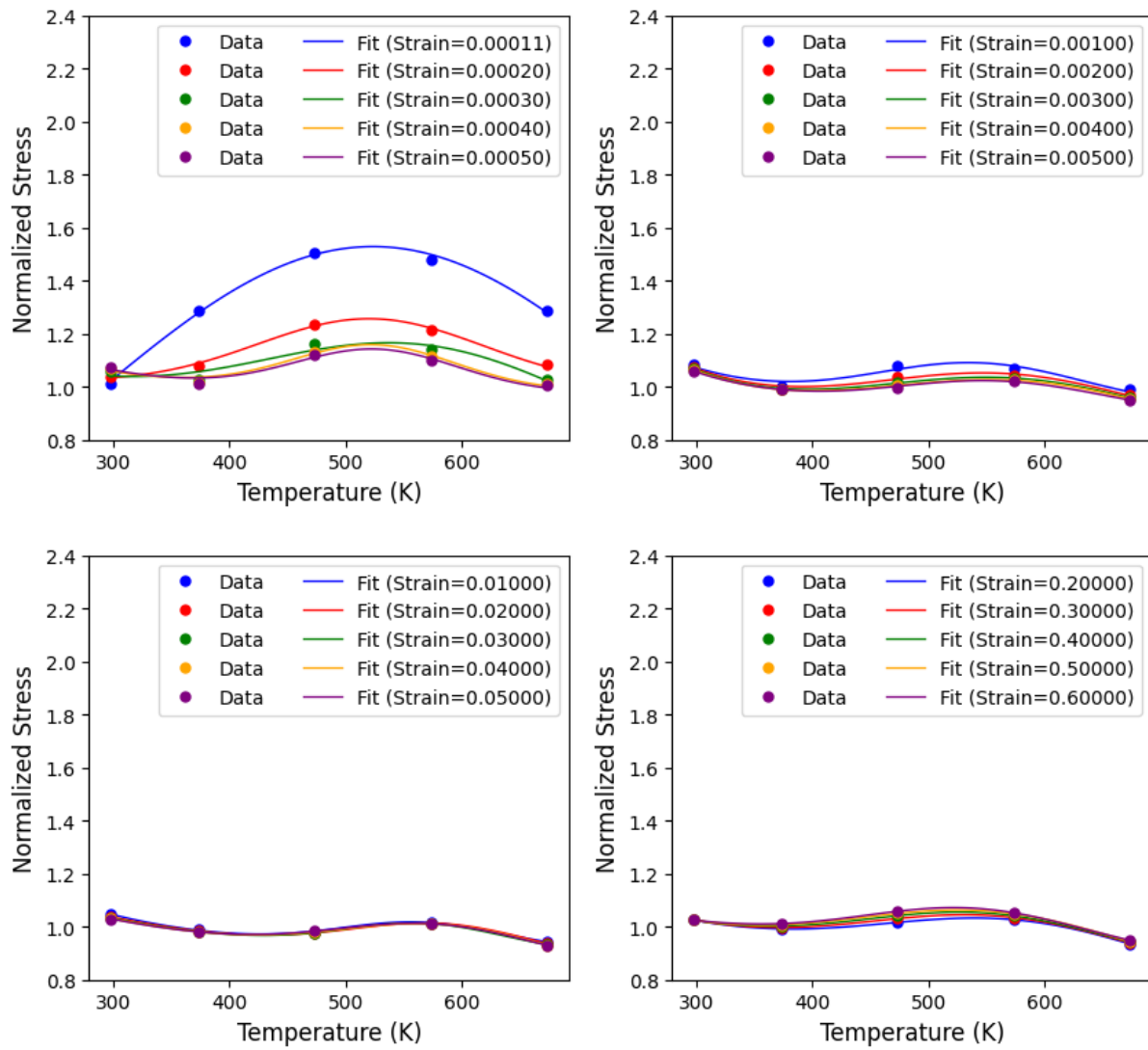


Figure 4-6. The prediction of six-parameter equation for the normalized stress in comparison with experimental and extrapolated data at strain-rate 0.1 considering different plastic strain levels.

4.1.2.2. Proposed nine-parameter function

As presented in Table 4-2, the nine-parameter function demonstrates higher accuracy in capturing the material behavior across all temperature ranges and strain-rates, with R-squared values consistently close to 1. Compared to the six-parameter function, the nine-parameter function provides better fitting quality at small strain values, such as 0.00011.

However, at intermediate strain values (from 0.01 to 0.04), as shown in the figure, although the accuracy remains, the fitted curve exhibits an unstable pattern with a

Results & Discussion

secondary peak occurring at 573.15 K. This behavior suggests that the nine-parameter function may be susceptible to overfitting, where the model captures the data too closely, leading to instability in the predicted response. Conversely, from a strain value of 0.05 onwards, the fitting quality becomes more stable, and the bell-shaped curve remains consistent across all strain values. This indicates that the nine-parameter function is better able to capture the material behavior in the plastic deformation regime, where the thermal softening and dynamic strain aging effects become more pronounced.

Overall, the nine-parameter function demonstrates higher accuracy in predicting the material's stress response, particularly at small and large strain values. However, the potential for overfitting at intermediate strain levels.

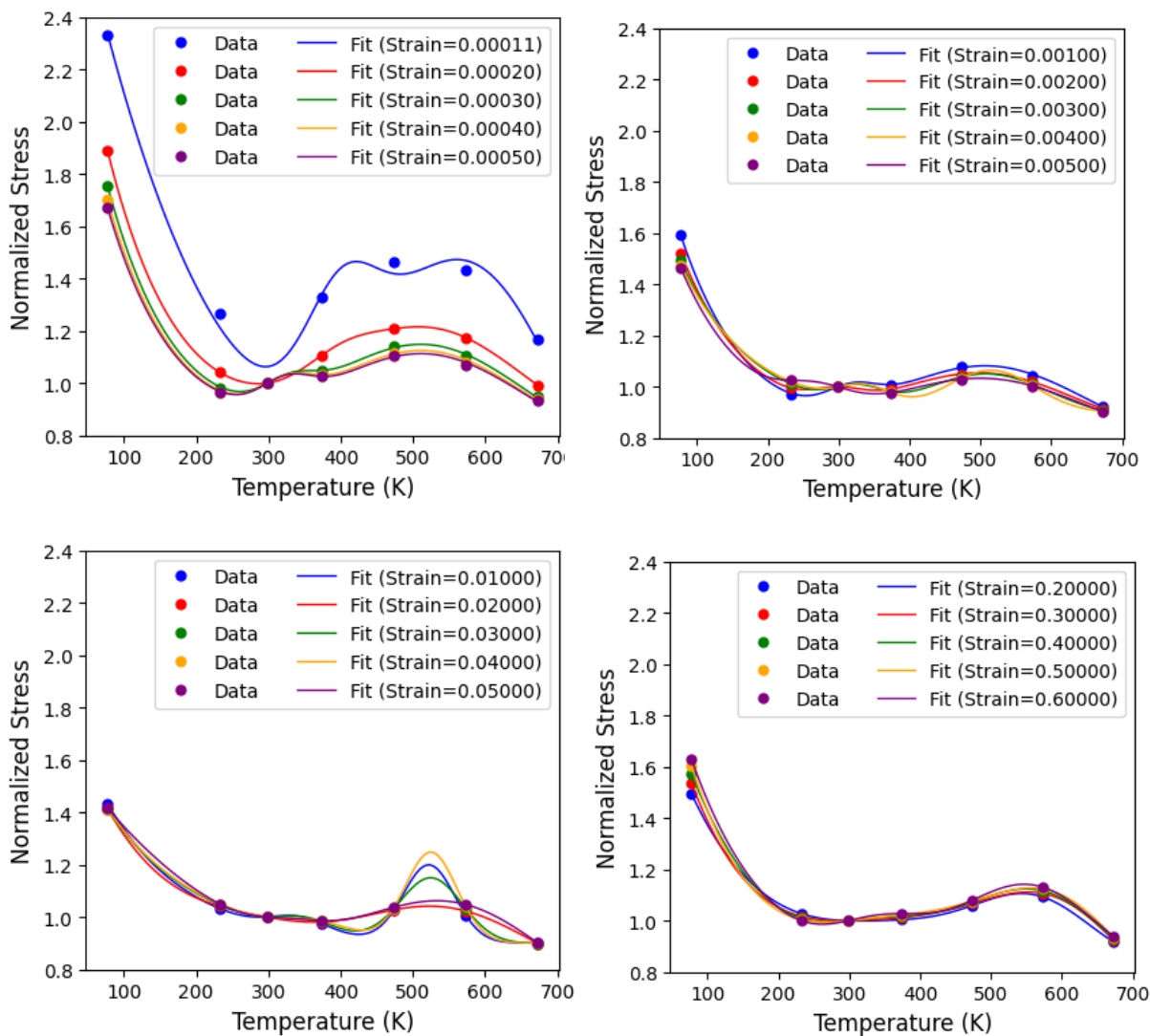


Figure 4-7. The prediction of nine-parameter equation for the normalized stress in comparison with experimental and extrapolated data at strain-rate 0.0001.

Results & Discussion

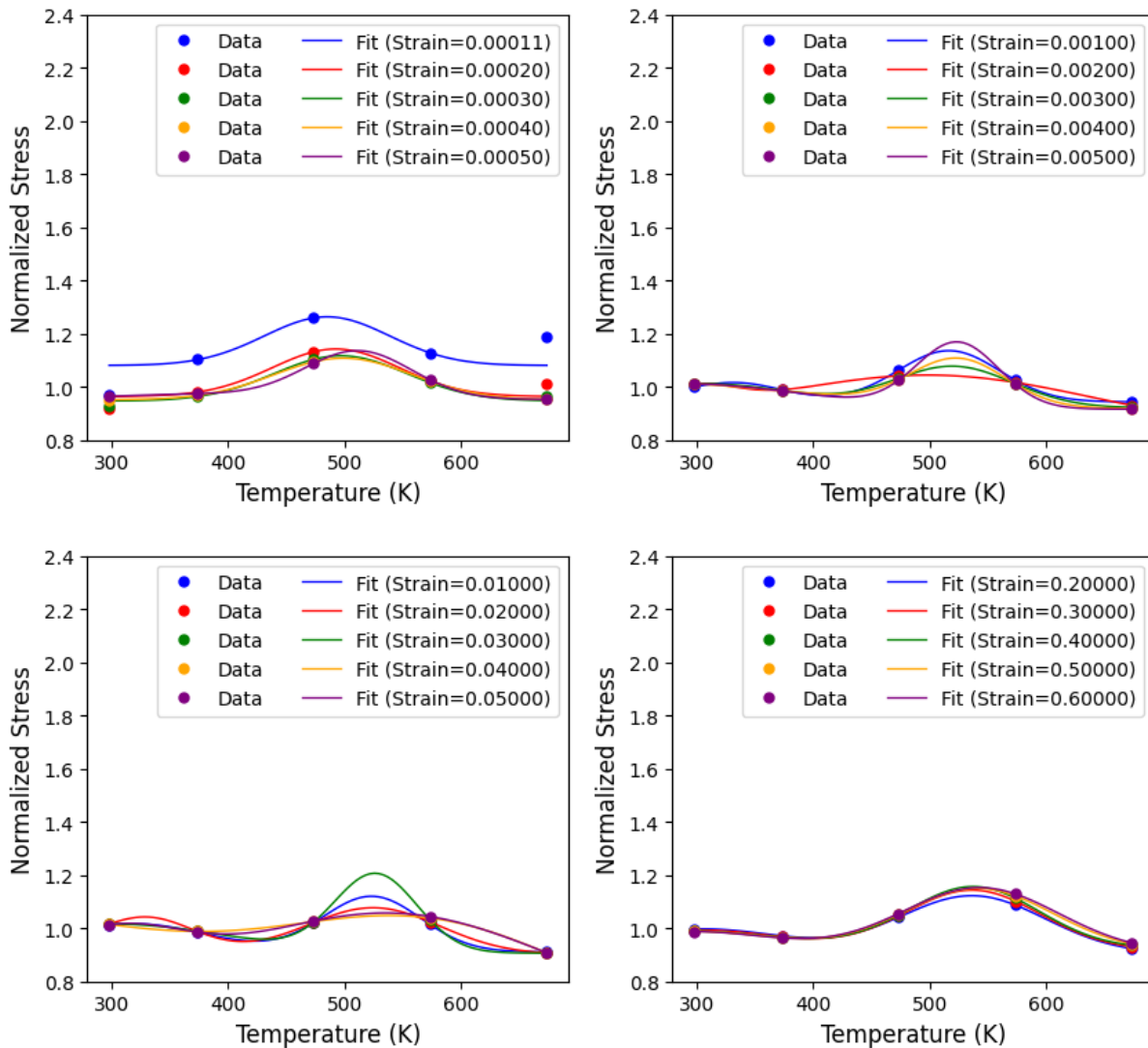


Figure 4-8. The prediction of nine-parameter equation for the normalized stress in comparison with experimental and extrapolated data at strain-rate 0.001.

Table 4-2: The r-squared value of prediction curves at different strain-rates of the nine-parameter function.

| R-squared / Strain-rate | 0.0001 | 0.001 | 0.01 | 0.1 |
|-------------------------|--------|--------|--------|--------|
| Smallest value | 0.99 | 0.483 | 0.975 | 0.91 |
| Largest value | 1 | 1 | 1 | 1 |
| Average value | 1 | 0.998 | 0.999 | 1 |
| R-squared values > 0.99 | 100% | 99.24% | 97.47% | 99.75% |

4.1.2.3. Thermal parameter calibration

The values of the thermal parameter C_1 for the six-parameter and nine-parameter functions are presented in Figure 4-9 and Figure 4-10 respectively. An important

Results & Discussion

observation is that the thermal parameters of the nine-parameter function exhibit significantly more variability across different strain-rates, making the calibration process more challenging. In contrast, the six-parameter function, although less precise, allows for a more manageable calibration process for the thermal parameters. This is a crucial consideration, as the goal is to develop a comprehensive model that can be easily applied across different strain levels and loading conditions.

Further analysis of Figure 4-9 reveals that the clearest trend in the thermal parameters is observed for the quasi-static strain-rate of 0.0001. This can be explained by the fact that Shen's study is focused on quasi-static loading conditions. Given these considerations, the decision is to proceed with calibrating the thermal parameters for the six-parameter function using the quasi-static strain-rate of 0.0001. This approach ensures a more manageable and reliable calibration process that can serve as a foundation for further model development and refinement. Therefore, the Equation (3-4) is used to calibrate the thermal parameters $C_{1\sim 6}$ at quasi-static strain-rate in the six-parameter equation.

The proposed thermal parameter calibration Equation (3-4) demonstrates good fitting performance. As illustrated in the Figure 4-11 and summarized in Table 4-3, the proposed equation provides a high fitting accuracy with the average r-squared values exceeding 0.99 for all six parameters. However, the function exhibits limited performance at smaller strain-rates, particularly for C_4 and C_6 , where it fails to capture initial drop and subsequent increase in thermal responses. This limitation highlights the complex nature of material behavior at microscopic deformation scales.

Table 4-3. The averaged r-squared value of fitted thermal parameters $C_{1\sim 6}$

| Thermal parameter | C_1 | C_2 | C_3 | C_4 | C_5 | C_6 |
|-------------------------|-------|-------|-------|-------|-------|-------|
| Average r-squared value | 0.998 | 0.996 | 0.990 | 0.975 | 0.966 | 0.915 |

Results & Discussion

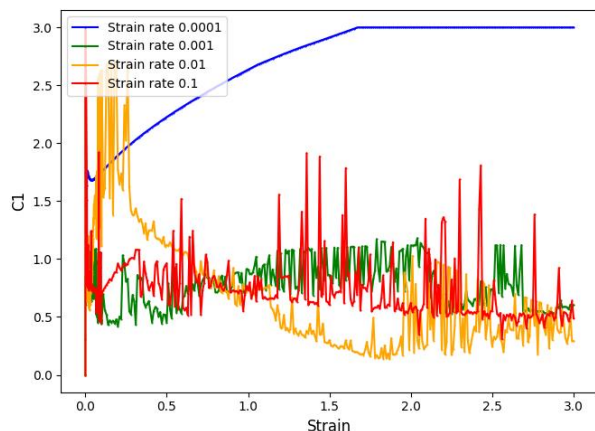


Figure 4-9. Calibrated thermal parameter C_1 of six-parameter function at different strain-rates.

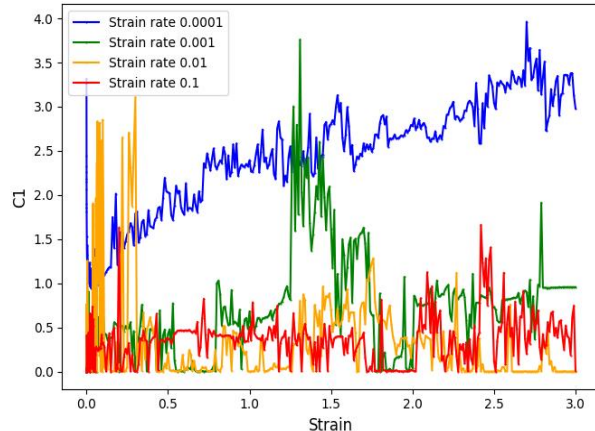
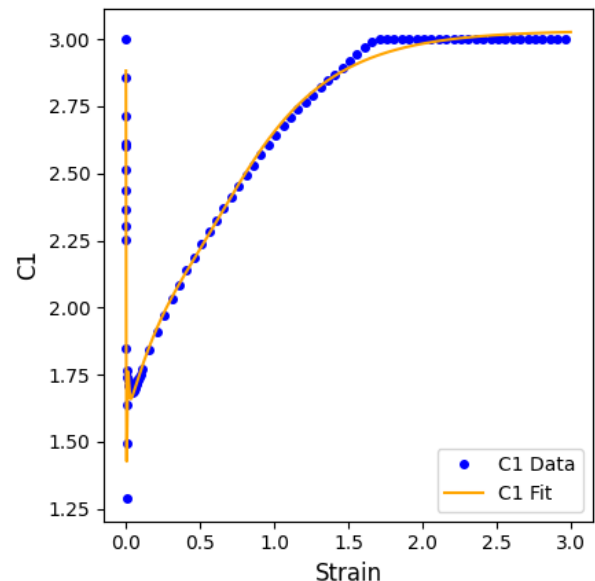
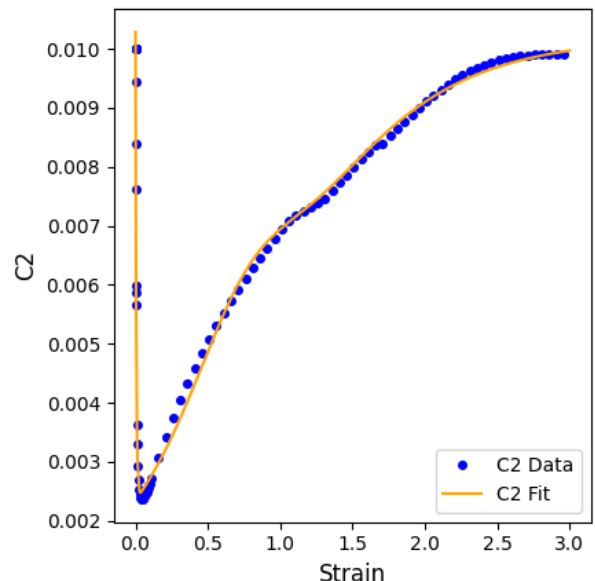


Figure 4-10. Calibrated thermal parameter C_1 of the nine-parameter function at different strain-rates.



(a) Thermal parameter C_1



(b) Thermal parameter C_2

Results & Discussion

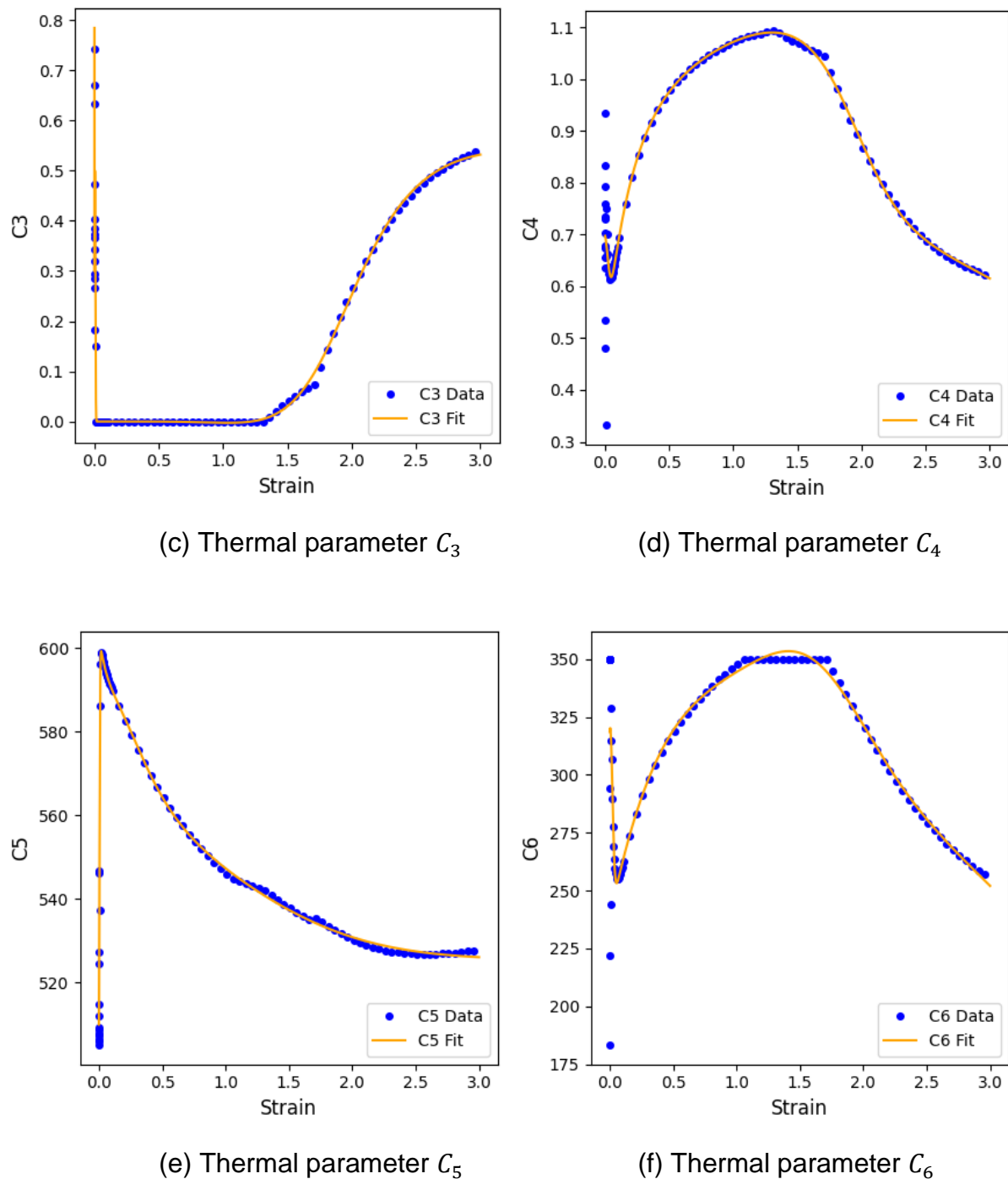


Figure 4-11. The prediction of thermal parameter $C_{1\sim 6}$ compared with calibrated values at strain-rate 0.0001 in the six-parameter equation.

4.1.2.4. Fitting validation

The complete thermal dependency calibration model integrates two complementary Equation (3-2) and (3-4). Validation results, presented in the Figure 4-12 demonstrate

Results & Discussion

high accuracy of the model's capability in capturing thermal effects, with an average r-squared value of 0.973. However, an observation of the proposed model is its performance variation across different strain ranges. As presented in the Figure 4-12, the model exhibits less accurate performance at small strains (below 0.012) and progressively stabilizes at higher strain values. This behavior aligns with the earlier observations in the thermal parameter calibration. Therefore, while the proposed model demonstrates significant potential in capturing thermal effects, there remains room for methodological refinement.

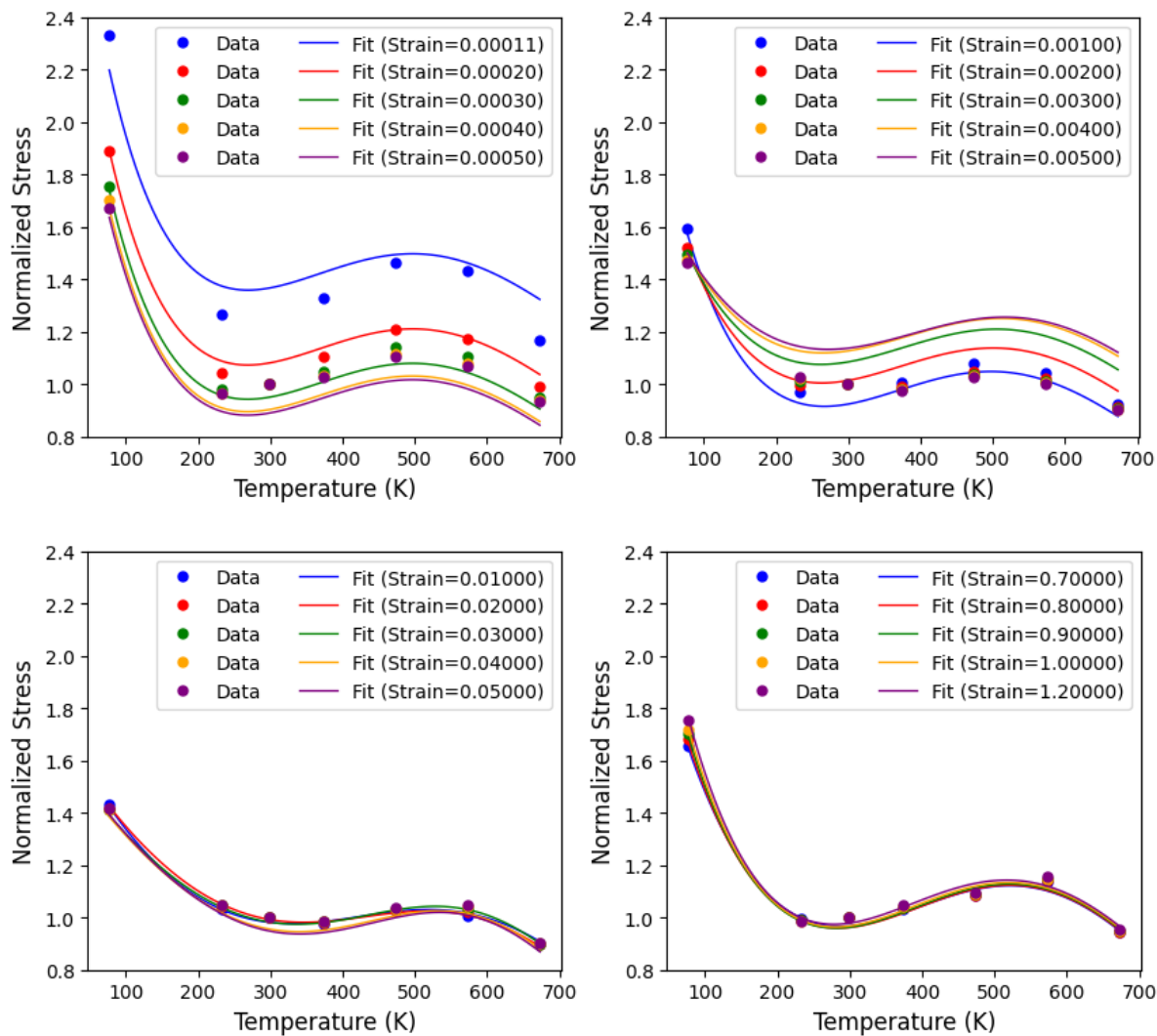


Figure 4-12. The validation thermal dependency model at strain-rate 0.0001.

This study develops and validates temperature dependency models including a thermal dependency function and a thermal parameter function with the validated r-squared value of 0.973. As for the thermal dependency function, Shen's six-parameter function and a proposed nine-parameter function are tested, offering different advantages and limitations. The six-parameter function demonstrates stable

Results & Discussion

performance in capturing material behavior trends, effectively representing thermal softening and dynamic strain aging effects across a broad temperature range. However, the function exhibits limitations in representing material behavior within the elastic region, particularly at smaller strain values. The nine-parameter function addresses the limitations of the six-parameter model. It provides better fitting accuracy across temperature and strain conditions, especially at small strain values. Simultaneously, the increased complexity introduced significant challenges in overfitting at intermediate strain levels and more complicated thermal parameter calibration process. An intermediate approach explores seven-parameter Equation (A-1) and (A-2) to bridge the gap between the six- and nine-parameter functions. The motivation is to address limitations in capturing material behavior at small strain values and regions. However, the additional parameter to the dynamic strain aging component does not significantly enhance model performance. Instead, it introduced redundancy without providing improvement in capturing material behavior. The result is summarized in the Table A-1 and Table A-2. This outcome may be attributable to the inherent characteristics of material responses in the elastic region.

4.1.3. Strain-rate dependency function parameter calibration

4.1.3.1. Previous students' proposal

The model proposed by previous students does not perform well since it assumes that the strain-rate sensitivity is simple. The results for R_squared values can be seen in Table 4-4. The best performance for this model is at 298.15K, illustrated in Figure 4-13. Since this method is ineffective and inaccurate, parameters are not calibrated. However, it is important to note that the parameters relationship evolving with strain is relatively easy to capture with mathematical functions. For example, Figure 4-14 shows C_1 and C_2 relationship with strain.

Table 4-4: The r-squared value of prediction curves at different temperatures of the previous students' proposed function

| R-squared/Temperature | 298.15K | 373.15K | 473.15K | 573.15K | 673.15K |
|-------------------------|---------|---------|---------|---------|---------|
| Smallest value | 0.412 | 1e-4 | 3.47e-5 | 0.011 | 0.024 |
| Largest value | 0.999 | 0.784 | 0.818 | 0.940 | 0.997 |
| Average value | 0.837 | 0.209 | 0.673 | 0.804 | 0.904 |
| R-squared values > 0.99 | 11.76% | 0% | 0% | 0% | 2.35% |

Results & Discussion

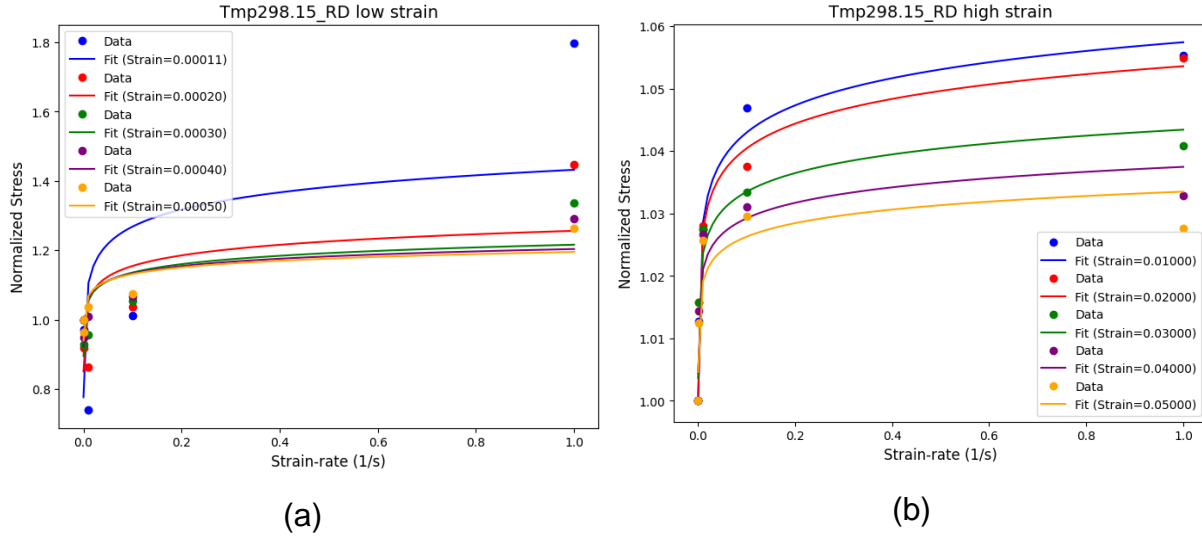


Figure 4-13: The prediction of proposed equation for the normalized stress in comparison with experimental data at 298.15K considering different plastic strain levels.

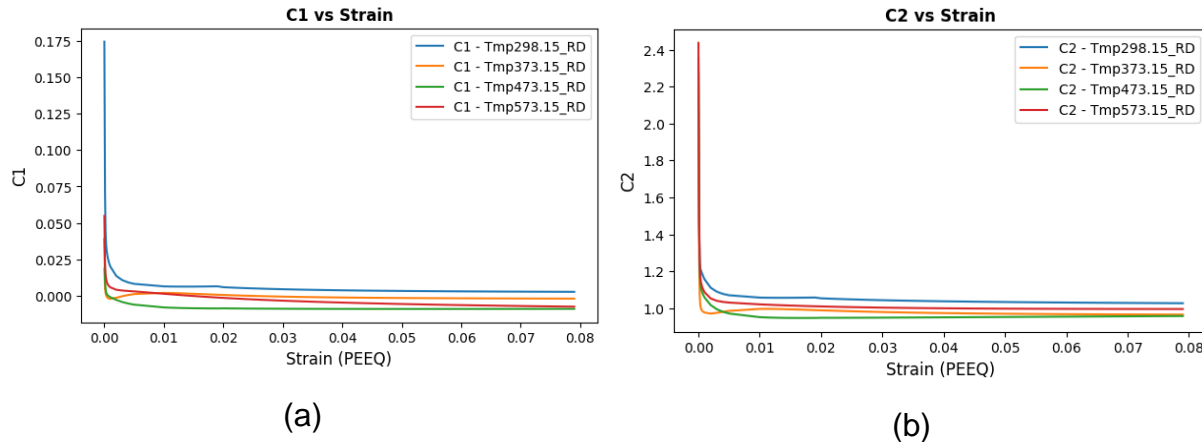


Figure 4-14: Calibrated strain-rate parameter C_i of the student proposed function at different temperatures.

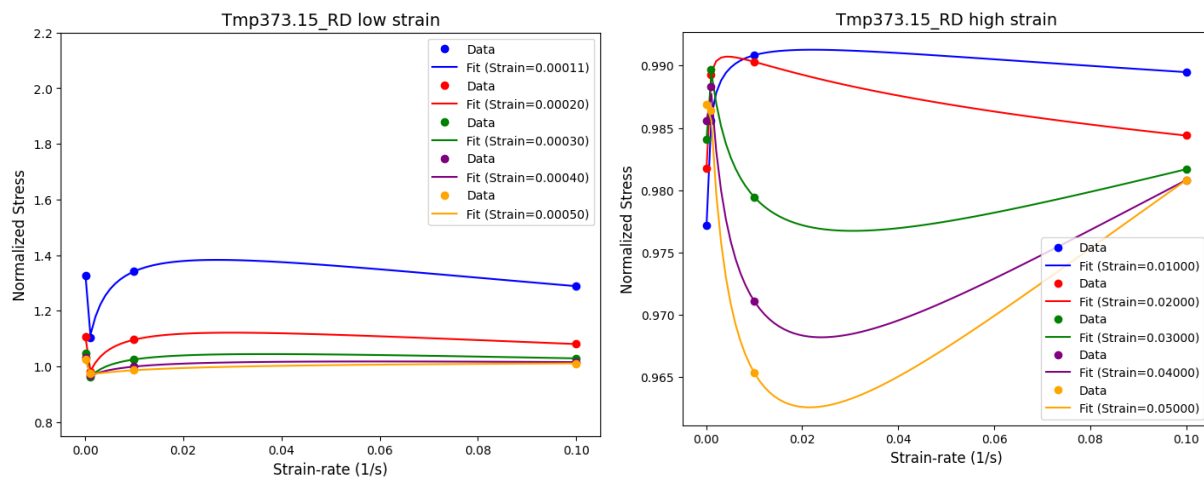
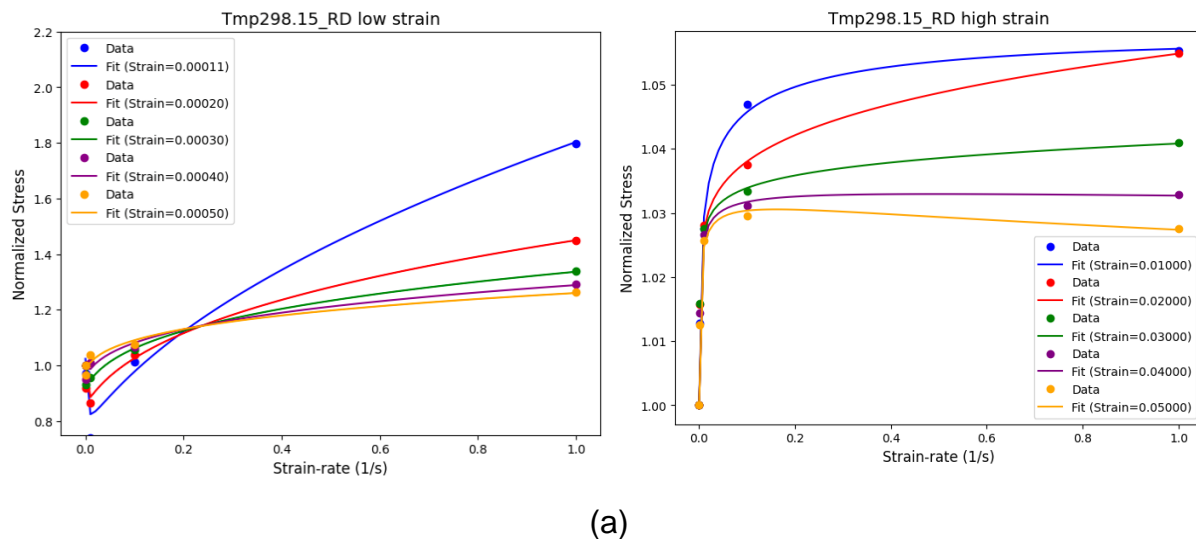
4.1.3.2. Proposed equation

The proposed function performs well across different temperatures as seen in Table 4-5. With the two additional terms to account for curvatures, the function can capture more complex non-linear behavior in comparison to the existing ones. The model output is consistent across low strain to high strain for different temperatures, as seen by the high average $r_{\text{_squared}}$ values. At room temperature, even though the 99th percentile is not as high, other metrics such as the smallest value and the average value suggest that the model can capture the data well. The results for each temperature are illustrated in Figure 4-15.

Results & Discussion

Table 4-5: The r-squared value of prediction curves at different temperatures of the proposed function.

| R-squared/Temperature | 298.15K | 373.15K | 473.15K | 573.15K | 673.15K |
|-------------------------|---------|---------|---------|---------|---------|
| Smallest value | 0.968 | 1 | 1 | 1 | 0.975 |
| Largest value | 1 | 1 | 1 | 1 | 1 |
| Average value | 0.993 | 1 | 1 | 1 | 0.999 |
| R-squared values > 0.99 | 85.88% | 100% | 100% | 100% | 98.82% |



Results & Discussion

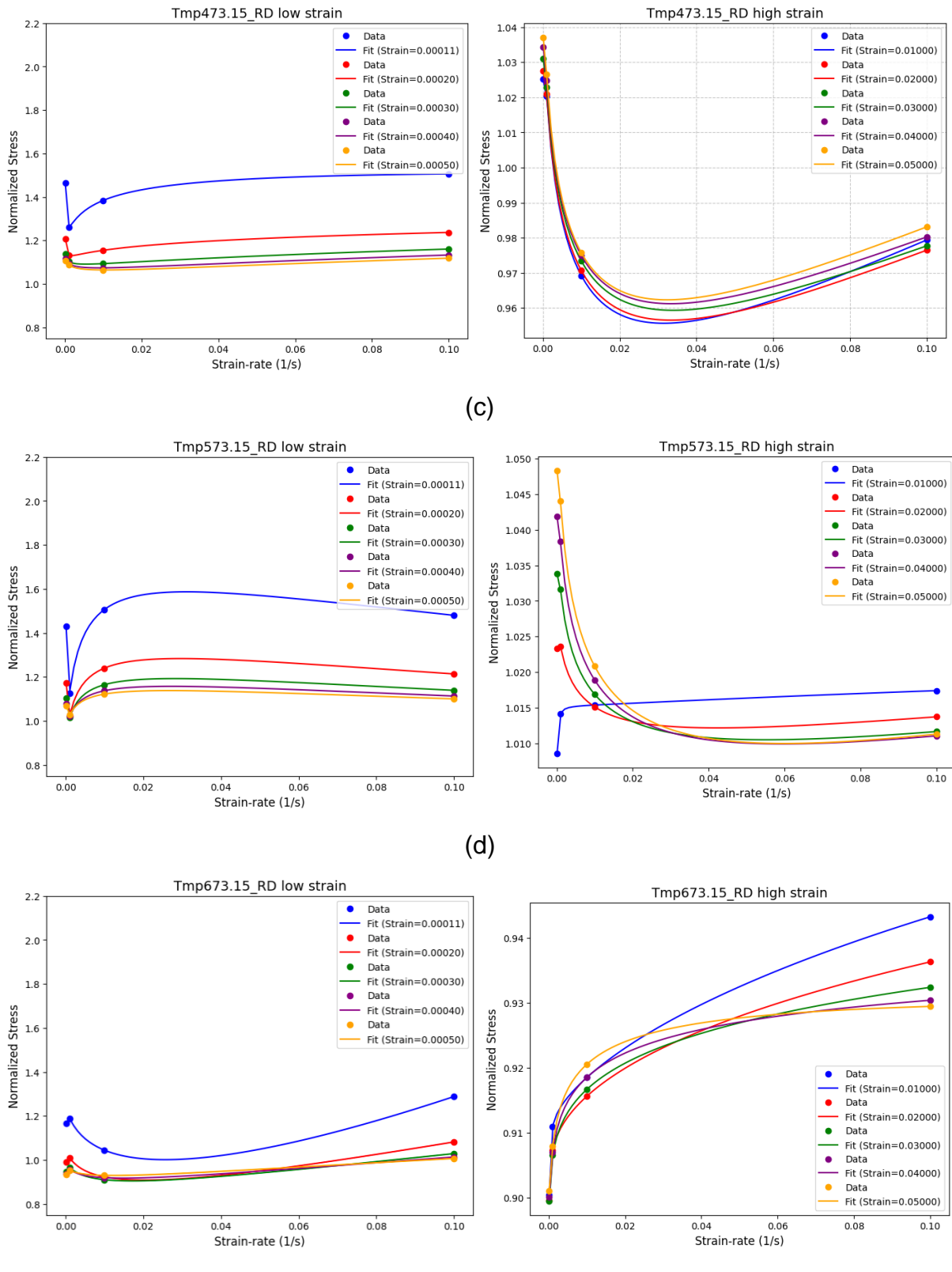


Figure 4-15: The prediction of proposed equation for the normalized stress in comparison with experimental data at different temperatures considering different plastic strain levels.

Results & Discussion

4.1.3.3. Strain-rate parameter calibration

With the given equations (3-8), the function indicates a good fit for different temperatures. The parameters for each function can be found in the Appendix. The r-squared values are summarized in Table 4-6. The best fitting quality are for C1 at 573.15K, C3 at 573.15K and C4 at 298.15K, 373.15K, 473.15K, 673.15K where the r-squared is perfect or almost perfect. Figure 4-16 shows the results for 473.15K parameter calibration fitting.

Table 4-6: R_squared value for strain-rate parameters calibration.

| R-squared | 298.15K | 373.15K | 473.15K | 573.15K | 673.15K |
|-----------|---------|---------|---------|---------|---------|
| C1 | 0.991 | 0.984 | 0.891 | 1.000 | 0.998 |
| C2 | 0.994 | 0.992 | 0.963 | 0.993 | 0.859 |
| C3 | 0.969 | 0.969 | 0.963 | 0.996 | 0.799 |
| C4 | 0.998 | 0.996 | 1.000 | 0.994 | 0.995 |

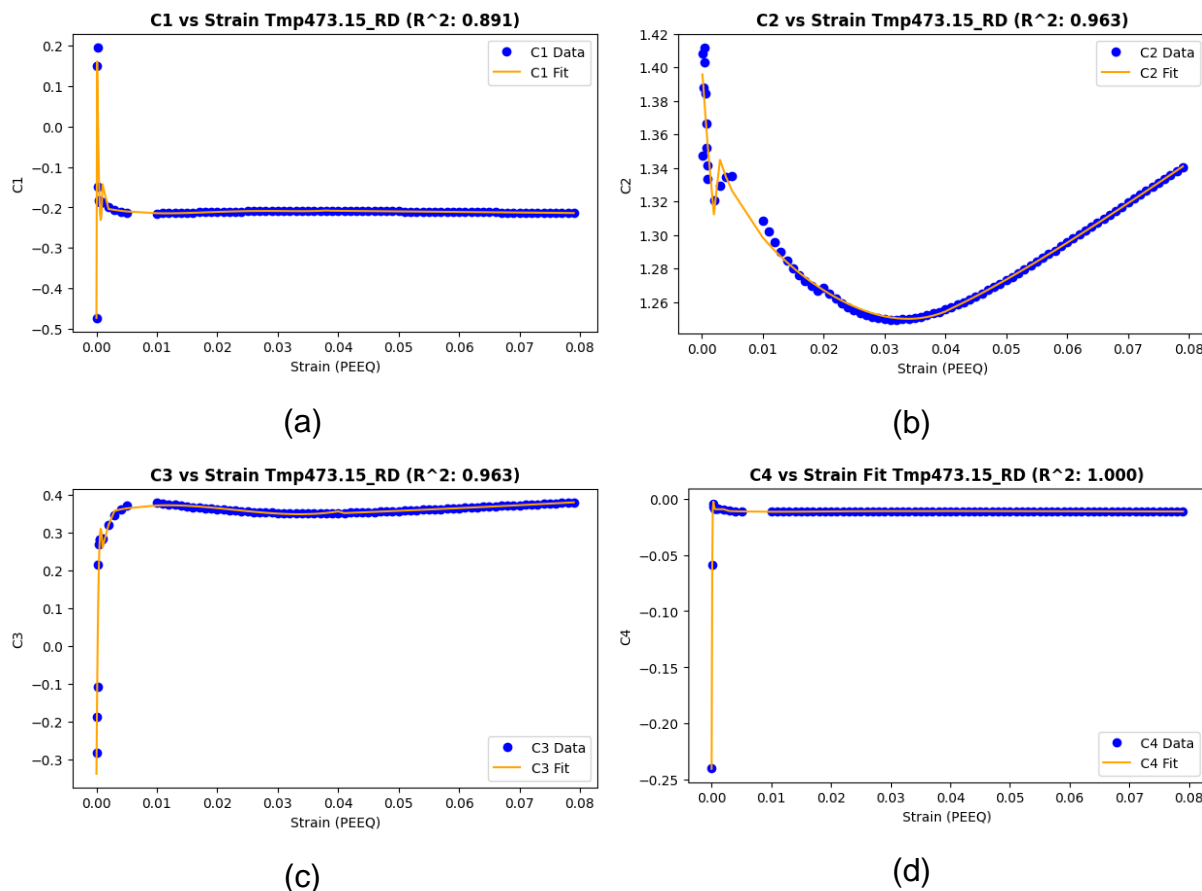


Figure 4-16: The prediction of strain-rate parameter $C_{1\sim 4}$ compared with calibrated values at 473.15K in the proposed equation.

Results & Discussion

4.1.3.4. Fitting validation

The final strain-rate dependency model consists of the main function (3-8) and the parameter functions (3-9), (3-10), (3-11), (3-12). In general, the results are satisfactory, illustrated in Table 4-7. The best performing temperature is 473.15K, shown in Figure 4-17, with very high r_squared value where strain is higher than 0.01. This shows that once the model has reached steady-state, it is easier to capture the trend of parameters for prediction.

Table 4-7: Strain-rate dependency validation r_squared.

| | 298.15K | 373.15K | 473.15K | 573.15K | 673.15K |
|-----------------|----------------|----------------|----------------|----------------|----------------|
| R_squared > 0.8 | 12.94% | 32.94% | 83.53% | 44.71% | 10.59% |

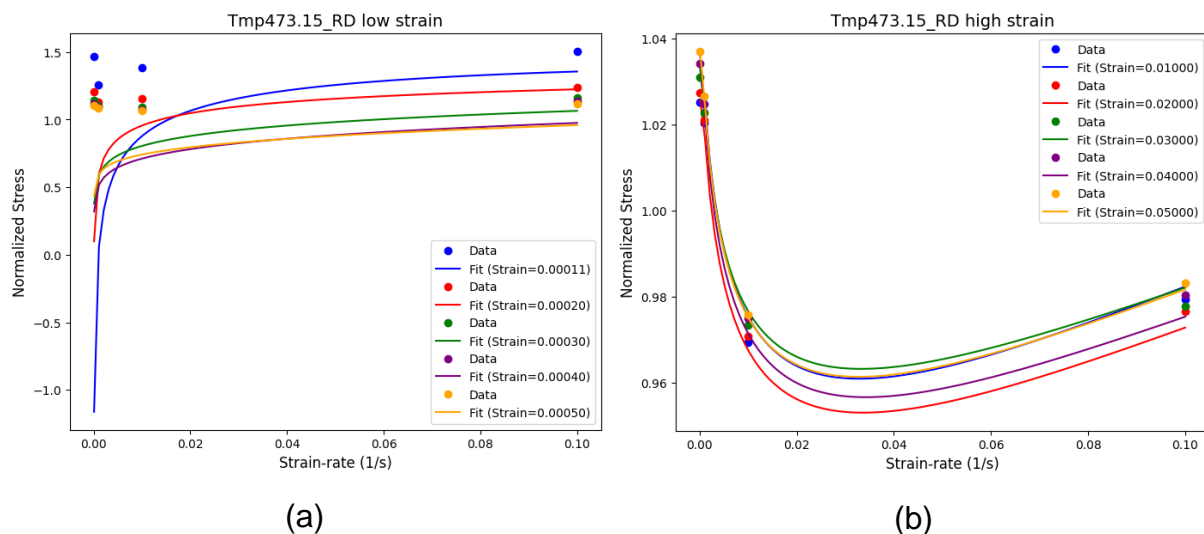


Figure 4-17: The validation of strain-rate dependency model at 473.15K.

Even though the fitting quality for both the main function and the parameters are excellent, the output is not good as expected. The main reason is the function oversensitivity with non-linear terms $\dot{\varepsilon}^{C_3}$ and $(\ln(\dot{\varepsilon}))^2$. Therefore, before this model can be applied in real life, it should be further refined.

To improve this model, the first method is to adjust the initial guess. The initial guess defines the optimization space for parameters selection and guides the curve_fit function. Choosing the initial guess contributes significantly to achieving the correct parameters. Another method is to further refine the calibrated parameter functions, especially for C_3 and C_4 where the function is most sensitive. The third suggestion is dynamic threshold to separate low, intermediate and high strain region for different

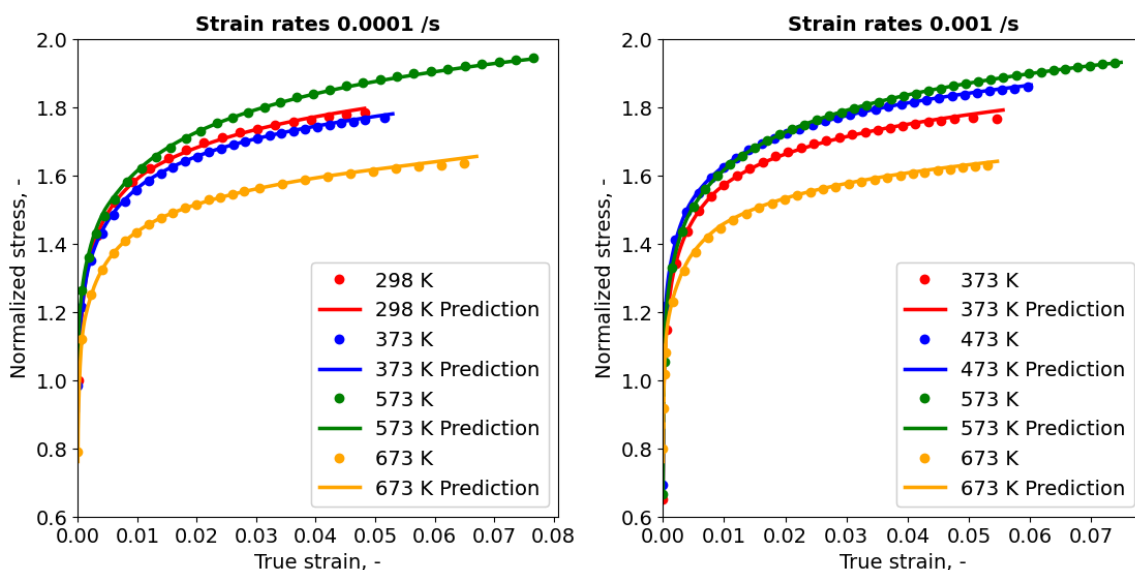
Results & Discussion

temperatures. Dynamic threshold allows the model to have more flexibility and partially adapt to the temperature effects on the material. This method is implemented by adding the thresholds as parameters that are optimized along with other mathematical parameters. With preliminary testing, the chosen dynamic threshold is the same as the suggested 0.002 and 0.04 while taking more computational time. However, as the initial guess for the threshold is updated, new results can be promising in the future.

4.2. Long Short-Term Memory model

The performance of the LSTM model is evaluated across different training set sizes to determine its ability to accurately predict stress-strain behavior under various conditions. Initially, the model is trained using only 8 flow curves. While the training accuracy is high, with an R^2 exceeding 0.98, the testing performance revealed significant gaps between the predicted and actual stress values. This indicated that the model lacked sufficient training data to learn the complex relationships present in the dataset.

As the size of the training set increased, the model's predictions improved significantly. With 12 flow curves, the model began to capture the general trends in the testing data, although some discrepancies remained. By using 15 flow curves, the testing accuracy increased further, with R^2 values nearing 0.97. However, the most notable improvement occurred when 16 flow curves were used for training. At this stage, the model achieved an R^2 greater than 0.99 on the training set and a highest R^2 above 0.99 for the testing set. This level of performance indicated a good balance between accuracy and generalization, making 16 flow curves the optimal training set size for this problem.



Results & Discussion

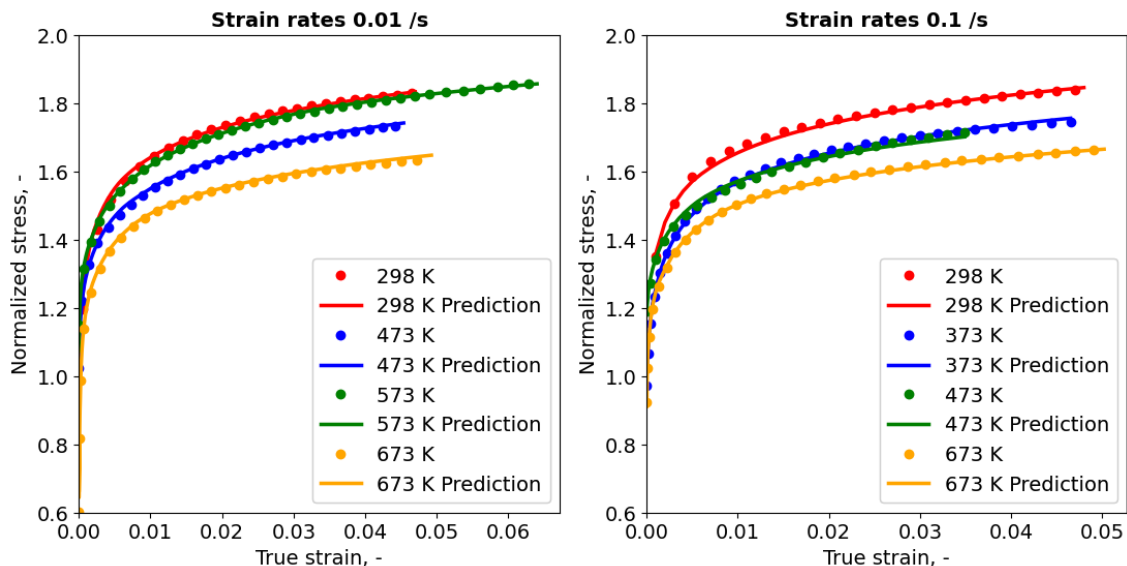
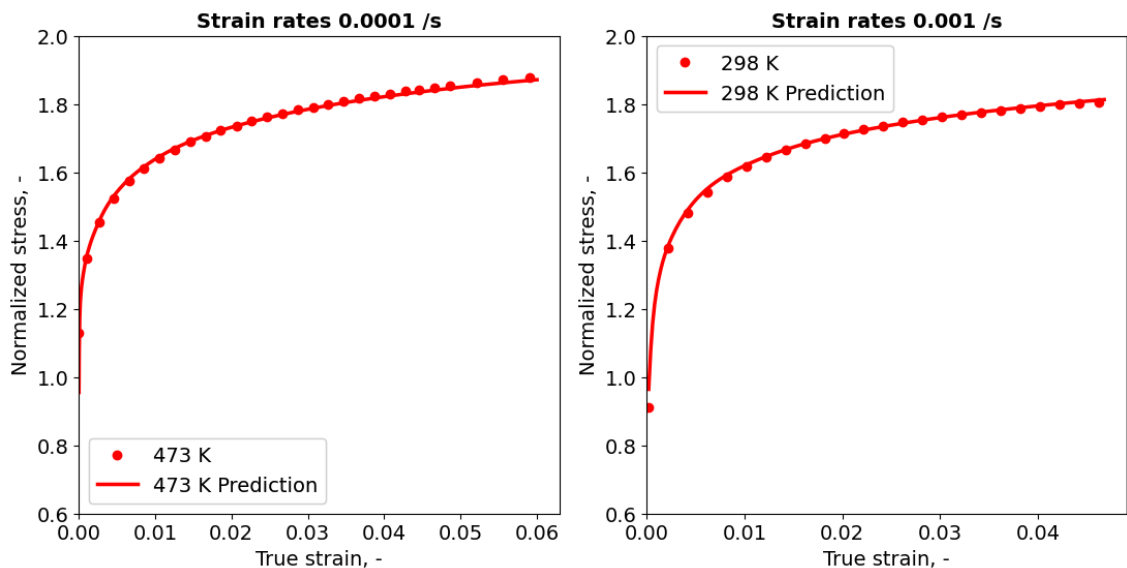


Figure 4-18: Model Predictions vs. Experimental Data for Training Set.



Results & Discussion

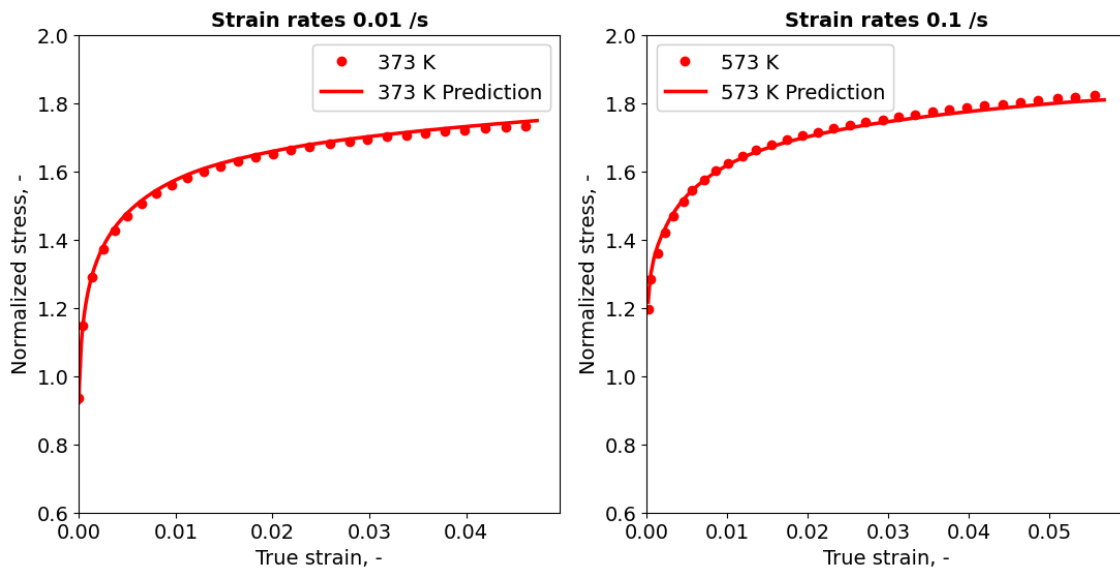


Figure 4-19: Model Predictions vs. Experimental Data for Testing Set.

When the model is trained with 19 flow curves, it achieved the highest R^2 values, exceeding 0.9956 on the testing set for specific cases. However, further analysis revealed signs of overfitting. While the model performed exceptionally well on the testing subset initially, testing on randomly selected flow curves showed a drop in R^2 to below 0.8 for some cases. This suggested that the model is memorizing patterns from the training data rather than generalizing to new conditions. As a result, 16 flow curves which represent all kinds of conditions is the most appropriate training set size to ensure stable and reliable predictions since the model predicts with R^2 is at least 0.88 and greater than 0.90 for almost testing cases. The LSTM model demonstrated its capability to capture the coupled effects of temperature and strain-rate on stress-strain behavior. For instance, at 300°C, the model successfully reproduced the phenomenon of dynamic strain aging (DSA), where stress levels remained elevated even at higher strain-rates. Similarly, the model captured the effects of thermal softening, where stress values decreased as the temperature increased. These results highlight the ability of the LSTM model to model the complex, nonlinear dependencies inherent in stress-strain relationships.

Despite its success, the model exhibited several limitations. Overfitting is a significant concern, particularly when the training set size approached the full dataset of 19 flow curves. This limitation underscored the need for a more diverse dataset to improve generalization. Furthermore, the interpretability of the LSTM model remained a

Results & Discussion

challenge. Understanding how the model made predictions, particularly in terms of physical phenomena (e.g. DSA), is not straightforward, which could limit its application in materials science. These limitations suggest that future work should focus on expanding the dataset to include a broader range of experimental conditions and exploring techniques to improve model interpretability.

In summary, the LSTM model achieved high accuracy in predicting stress-strain relationships, with an optimal training set size of 16 flow curves yielding consistent and reliable results. The model effectively captured key material behaviors, such as thermal softening and dynamic strain aging, demonstrating its potential for modeling coupled strain-rate and temperature dependencies. However, challenges such as overfitting and limited dataset diversity highlight areas for future improvement.

4.3. Validation

4.3.1. Machine Learning model

Figure 4-18 illustrates the simulated data for 773.15K and quasi-static strain-rate at rolling direction. As can be observed, three geometries can be obtained from the simulation: NDBR6, NDBR20r, and NDBR50f. Looking at the plot, the simulated flow curves do not align well with the experimental data, however, some interesting insights can be acquired.

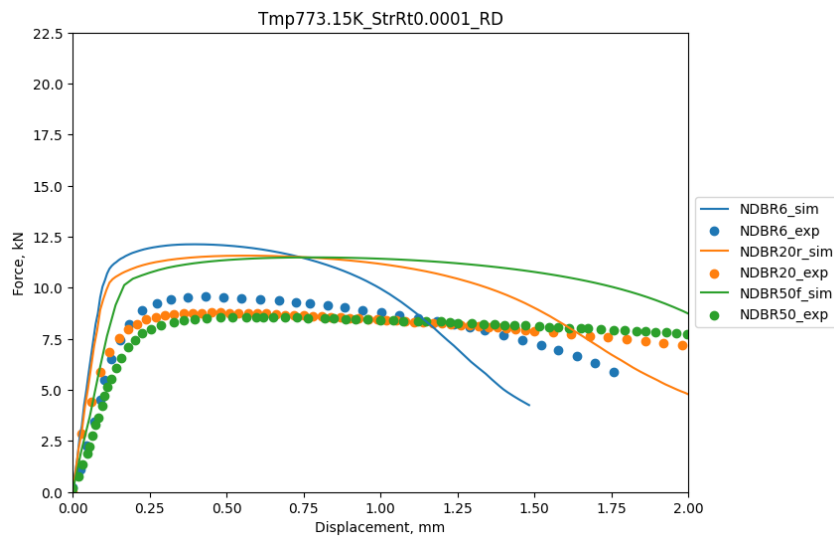


Figure 4-20: Simulation result for 773.15K, StrRt 0.0001 at RD.

Overall, the simulated force-displacement lines generally follow the trend of the experimental data points. They seem to align well with the early displacement range. However, deviations begin to happen at around displacement of 0.25mm, where the simulation overestimates the force compared to the experimental data. While this discrepancy is not entirely unexpected, it is worth further investigation. One possible explanation for the anomaly in the data at 773.15K is that the data do not follow the overall trend observed in other experimental conditions.

This would be better understood if all the experimental force-displacement data for the geometries of NDBR6, NDBR20r, and NDBR50f at different temperature conditions were plotted at a strain-rate of 0.0001. The behavior of the data at 773.15K in the context of the broader dataset provides some insight into why the simulation appears to deviate from the experimental results at this condition.

Results & Discussion

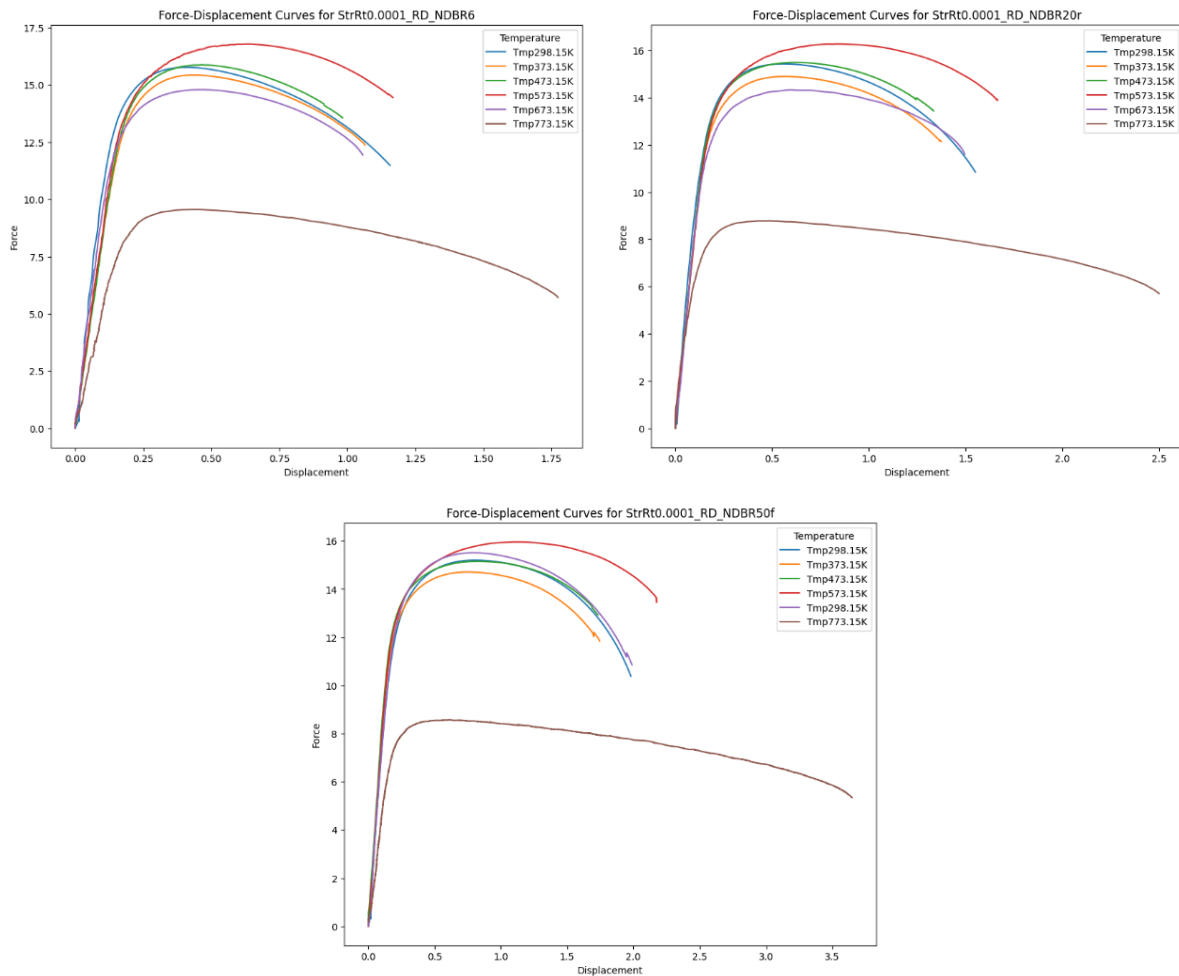


Figure 4-21: Comparison of Experimental Force-Displacement Curves of all Temperature at quasi-static strain-rate for geometries: a) NDBR6, b) NDBR20r, c) NDBR50f.

While the simulated data generally follows the overall trend, the LSTM model might not be ready for conditions with significant anomalies, as shown in Figure 4-21 a) to c). This indicates that further reinforcement may be necessary for the model to be utilized in actual cases.

4.3.2. Constitutive Model

Figure 4-22 presents the force-displacement curves obtained from the simulation using material inputs taken from the calibrated temperature function. These curves give a better fit with the experimental data compared to Figure 18. However, discrepancies are still visible in all geometries, especially at around the peak:

- NDBR6 significantly overpredicts the peak force compared to the experimental data.
- NDBR20r gives results closer to the experimental data, having only a slight overprediction with respect to the peak.

Results & Discussion

- NDBR50f has the best peak force performance, which gives a good balance between prediction accuracy and force estimation.

Whereas the simulated data for NDBR6 after the peak dramatically reflects a sharp decline, instead of decreasing steadily like the experimental data. The other two follow the general trend in experimental findings, although it also gives some deviation towards the end.

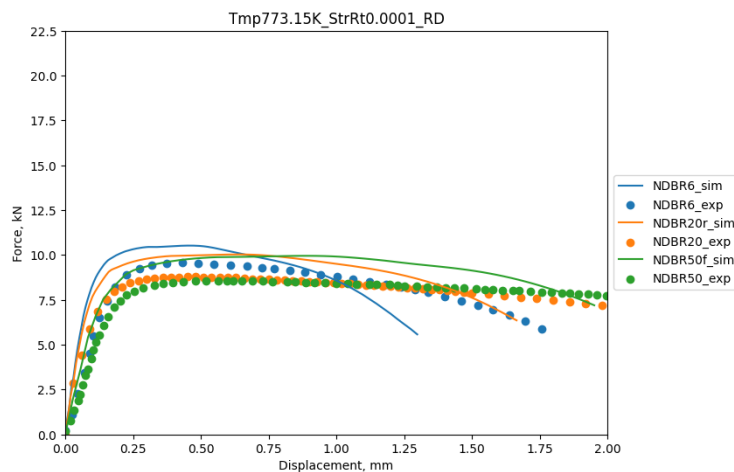


Figure 4-22: Comparison of experimental and simulated force-displacement curves for DP1000 steel at 773.15k and strain-rate 0.0001 (rolling direction), simulated using temperature dependency function.

In the unified model method, we validated the constitutive model using data obtained from calibrated temperature and strain-rate functions to predict the values of normalized stress at 473.15K and strain-rate of 0.001. Analysis was done only up to the strain value of 0.3, because beyond this, the strain-rate function is unable to give reliable predictions.

When evaluating the performance of each module separately, both the calibrated strain-rate function and the temperature function demonstrate strong predictive capabilities, as shown in Figure 4-21. From Figure 4-23(a), the strain-rate function provide an accurate fit to the experimental data, with the only notable limitation being its inability to capture the initial experimental data point precisely. On the other hand, Figure 4-23 (b) shows that the temperature function effectively predicts the stress-strain behavior during the early deformation stages. However, minor deviations become apparent around a strain value of 0.1, where the predicted stress slightly exceeds the experimental data in the later stages.

Results & Discussion

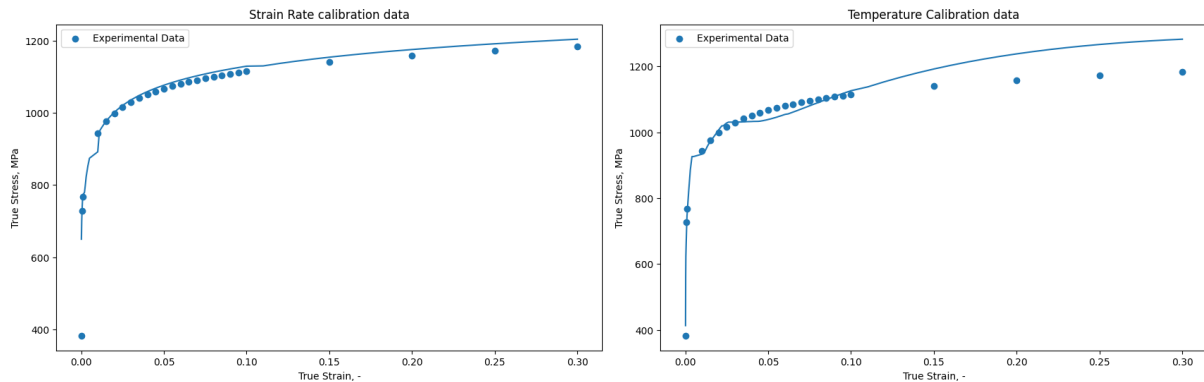


Figure 4-23: Stress-Strain Comparison at 473.15K, Strain-rate 0.001 for a) Strain-rate function, b) Temperature function

Overall, both functions portray very good prediction accuracy and the material behavior within their range. The remaining challenge relates to how these functions must be combined into one homogeneous model that can represent the interaction of strain-rate and temperature more comprehensively.

Initially we tried to fit the strain-rate of 0.001 in Equation (3-14) to find the value of β . However, as this equation was intended to find β at higher strain-rate, we could not find a desirable value for $\beta_{0.01}$. Instead, we can obtain the value for β at strain-rate by looking at this graph:

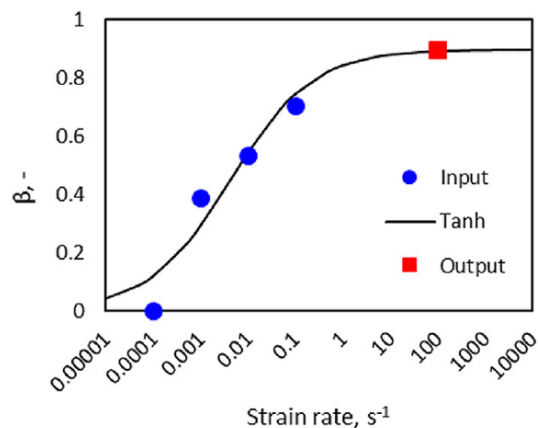


Figure 4-24: The Taylor-Quinney coefficient as the function of strain-rate, (Liu et al., 2020)

We can observe from Figure 4-24 that the second blue dot from the left actually represents the value of β at strain-rate of 0.001. Therefore, we can assume that $\beta_{0.01}$ is approximately 0.04. However, when we plug in the value of $\beta_{0.01}$ into Equation

Results & Discussion

(3-13) along with the generated stress from both temperature and strain-rate modules, the result does not look really appealing.

This would consequently suggest that the current way of integrating the temperature and strain-rate modules into a common framework needs further refinement. Future work may be done on recalibration of β at low strain-rates, or explore alternative means to combine the two components to achieve a better capturing of their interactive effects; such improvements would extend the predictive capability over more extensive range conditions.

4.4. Comparison between constitutive model and LSTM model

The accuracy of the constitutive model and the machine learning (LSTM) model demonstrates their respective strengths in different aspects of material modeling. The constitutive model achieves an R-squared value of 0.972 for temperature calibration and 0.82 for strain rate calibration. While these values indicate a solid performance in capturing material behavior under varying conditions, the LSTM model outperforms it with an R-squared value of 0.99. This higher accuracy suggests that the LSTM model is better suited for tasks requiring precise predictions across a range of variables, especially when dealing with complex, non-linear dependencies.

The development effort required for the two models is markedly different. The constitutive model involves separate calibration steps for temperature and strain rate, which demand significant time and expertise. Additionally, the process is iterative, requiring numerous trials and errors to optimize the initial guesses and determine the appropriate function shapes. This effort typically involves a team of 1 developer and 2 assistants for both calibration stages. On the other hand, the LSTM model reduces the complexity of the development process. While it also requires some experimentation to identify an optimal training-to-testing ratio, the process is less resource-intensive, requiring only 1 developer and 1 assistant. This reduction in effort makes the LSTM model more accessible, particularly for teams with limited resources or expertise in traditional constitutive modeling.

Development time is a critical factor in selecting a modeling approach, and the LSTM model offers a significant advantage in this regard. The constitutive model requires approximately 8 weeks to complete, reflecting the time-intensive nature of calibration and optimization. In contrast, the LSTM model can be developed in just 3 weeks, highlighting its efficiency in leveraging machine learning algorithms to automate and streamline much of the modeling process. This reduced timeline makes the LSTM model particularly appealing for applications with tight deadlines or when rapid prototyping is needed.

The usability of the two models differs significantly due to their underlying nature. The constitutive model provides clear physical meaning and interpretability, which are valuable for engineers and researchers seeking to understand the underlying material

Results & Discussion

behavior. Its straightforward mathematical framework also makes it easier to use in practical applications once the calibration is complete. However, the LSTM model lacks this physical interpretability, functioning instead as a black-box model. While this limits its ability to provide insights into the physical mechanisms, it offers advantages in ease of deployment and adaptability to new datasets. For practical use, some deployment steps are necessary to integrate the LSTM model into workflows, but this is balanced by its superior accuracy and faster development time.

In conclusion, the choice between the constitutive model and the LSTM model depends on the specific requirements of the application. The constitutive model is ideal for scenarios where physical interpretability and an understanding of material behavior are critical. However, it is resource- and time-intensive, requiring extensive calibration and expertise. In contrast, the LSTM model offers a faster, more efficient solution with higher accuracy, making it a practical choice for applications where interpretability is less important but speed and precision are paramount. For teams with prior knowledge of machine learning, the LSTM model is particularly advantageous, offering a streamlined development process with minimal resource requirements. Ultimately, the trade-offs between interpretability, accuracy, and development effort must be carefully considered when selecting a modeling approach.

5. Conclusions and Outlooks

The goal of this research is to develop and validate constitutive and machine learning-empowered models to predict the mechanical behavior of high-strength-steel (HSS), specifically DP1000, under a variety of forming conditions. Two different modeling approaches were attempted: first, temperature and strain-rate dependencies were modeled independently using an advanced constitutive law, while a Long Short-Term Memory machine learning-based model was adopted for data-driven predictions:

- The **temperature-dependent module** provided very good predictive performance. It effectively captured thermal softening and dynamic strain aging phenomena, showing high reliability in the moderate strain range.
- The **strain-rate-dependent module** gave strong results over low and high strain-rates, but it requires further refinement in order to handle transitions within the intermediate strain regions.
- The **LSTM-based machine learning model** reaches to a remarkable prediction accuracy of $r_{\text{squared}} = 0.99$, which is very accurate and can capture the material behavior without explicit parameterization. The model has proved to be a flexible predictive tool, yet challenges of overfitting and limited interpretability suggest further areas of improvement.

Based on these findings, the following recommendations and prospects could be proposed for further enhancing the models and their application:

- Applications:
 - o The **temperature** and **strain-rate modules** can be applied in finite element simulation of forming processes in order to design lightweight, yet crash-resistant automotive components.
 - o The **LSTM model** can prove to be very promising for predictive modeling in small-size experiments.
- Limitations and Future Refinements:
 - o The **temperature module** is very accurate in most of the moderate conditions but needs refinements to better capture the extreme temperature effects and coupling phenomena.

Conclusions and Outlooks

- The **strain-rate module** would be better off with dynamic calibration strategies in order to enhance performance in transitional strain regions.
- The **LSTM model** can be improved by increasing the size of the training dataset and incorporating interpretability mechanisms, such as attention layers or hybrid physics-based approaches.

By addressing these challenges, the two models developed in this project can significantly advance for better predictive capabilities to determine sustainable manufacturing route for the automotive industry. Their successful implementation paves the way for further innovation in modeling high-strength steels and beyond.

6. Personal evaluation

This project was a unique and priceless experience that our team had; it was one of the most significant group projects our team has ever completed during our studies at Aalto University. During this course, we gain technical skills in teamwork through Python and Abaqus and high-performance computing on Puhti. Each of these tools is very important to deal with data processing, simulation work, and automation that saves time while doing a lot of repetitive tasks. We also tried using the machine learning technique, namely the LSTM model, to predict material behavior. This required us to understand how LSTM would be combined with traditional material modeling in order to extend the paradigm of contemporary computational techniques.

The project also gave us an avenue to enforce teamwork and problem-solving skills. Being an intensive class, we had to make quite sure that it entailed effective communication, coordination, and collaboration; thereafter, we worked closely in the division of tasks and overcoming various challenges. The experience not only reinforced our technical skills but also our productive teamwork.

We would like to thank the guidance and arrangement by Professor Lian. His comments during mid-term and final workshops gave us many valuable hints for refinement, and the seminars he hosted really provided an excellent opportunity to engage with leading experts in the field. We also appreciate his effort in setting a good and motivating environment-like offering pizza and coke during the final workshop.

We would also like to express our most profound appreciation to our advisor, Zinan, for the constant support and patience she has shown throughout this project. Her knowledge and experience were exceedingly helpful in guiding us through problems that arose, while her encouragement has played a significant role in moving us along on this project.

Lastly, we would like to show appreciation for the effort and devotion invested by each member of the team. The collaboration and mutual support that were present in the group were crucial for us in allowing successful completion of the project, which proved to be an enriching experience for all of us.

References

- Bai, Y., Wierzbicki, T., 2008. A new model of metal plasticity and fracture with pressure and Lode dependence. *Int. J. Plast.* 24, 1071–1096. <https://doi.org/10.1016/j.ijplas.2007.09.004>
- Benabou, L., 2021. Development of LSTM Networks for Predicting Viscoplasticity With Effects of Deformation, Strain, and Temperature History. *J. Appl. Mech.* 88, 071008. <https://doi.org/10.1115/1.4051115>
- Dabbaghi, F., Tanhadoust, A., Ogunsanya, I.G., 2024. Pruning Long Short-Term Memory: A Model for Predicting the Stress–Strain Relationship of Normal and Lightweight Aggregate Concrete at Finite Temperature. *Fire Technol.* <https://doi.org/10.1007/s10694-024-01606-9>
- Goodfellow, I., Bengio, Y., Courville, A., 2016. Deep learning, Adaptive computation and machine learning. The MIT press, Cambridge, Mass.
- Gorji, M.B., Mozaffar, M., Heidenreich, J.N., Cao, J., Mohr, D., 2020. On the potential of recurrent neural networks for modeling path dependent plasticity. *J. Mech. Phys. Solids* 143, 103972. <https://doi.org/10.1016/j.jmps.2020.103972>
- Hodson, T.O., 2022. Root-mean-square error (RMSE) or mean absolute error (MAE): when to use them or not. *Geosci. Model Dev.* 15, 5481–5487. <https://doi.org/10.5194/gmd-15-5481-2022>
- Liu, W., Lian, J., Münstermann, S., 2019. Damage mechanism analysis of a high-strength dual-phase steel sheet with optimized fracture samples for various stress states and loading rates. *Eng. Fail. Anal.* 106, 104138. <https://doi.org/10.1016/j.engfailanal.2019.08.004>
- Moradkhani, F., Fibich, C., Fränzle, M., 2023. Verification of LSTM Neural Networks with Non-linear Activation Functions, in: Rozier, K.Y., Chaudhuri, S. (Eds.), NASA Formal Methods, Lecture Notes in Computer Science. Springer Nature Switzerland, Cham, pp. 1–15. https://doi.org/10.1007/978-3-031-33170-1_1
- Mozaffar, M., Bostanabad, R., Chen, W., Ehmann, K., Cao, J., Bessa, M.A., 2019. Deep learning predicts path-dependent plasticity. *Proc. Natl. Acad. Sci.* 116, 26414–26420. <https://doi.org/10.1073/pnas.1911815116>
- Pillai, P., Pal, P., Chacko, R., Jain, D., Rai, B., 2021. Leveraging long short-term memory (LSTM)-based neural networks for modeling structure–property

References

- relationships of metamaterials from electromagnetic responses. *Sci. Rep.* 11, 18629. <https://doi.org/10.1038/s41598-021-97999-6>
- Sase, K., Shibuta, Y., 2023. Prediction of microstructure evolution at the atomic scale by deep generative model in combination with recurrent neural networks. *Acta Mater.* 259, 119295. <https://doi.org/10.1016/j.actamat.2023.119295>
- Shen, F., Münstermann, S., Lian, J., 2020. An evolving plasticity model considering anisotropy, thermal softening and dynamic strain aging. *Int. J. Plast.* 132, 102747. <https://doi.org/10.1016/j.ijplas.2020.102747>
- Stryker, C., 2024. What is a recurrent neural network (RNN)?
- Swift, H.W., 1952. Plastic instability under plane stress. *J. Mech. Phys. Solids* 1, 1–18. [https://doi.org/10.1016/0022-5096\(52\)90002-1](https://doi.org/10.1016/0022-5096(52)90002-1)
- Chahaoui, O., Soltani, H., & Matougui, N. (2021). Application of associated and non-associated flow metal plasticity for F.S.S sheet [Article]. *Defect and Diffusion Forum*, 406, 473-480. <https://doi.org/10.4028/www.scientific.net/DDF.406.473>
- Lian, J., Shen, F., Jia, X., Ahn, D.-C., Chae, D.-C., Münstermann, S., & Bleck, W. (2018). An evolving non-associated Hill48 plasticity model accounting for anisotropic hardening and r-value evolution and its application to forming limit prediction. *International Journal of Solids and Structures*, 151, 20-44. <https://doi.org/https://doi.org/10.1016/j.ijsolstr.2017.04.007>
- Shen, F., Lian, J., & Münstermann, S. (2018). A comparative study on the forming limit diagram prediction between Marciniak-Kuczynski model and modified maximum force criterion by using the evolving non-associated Hill48 plasticity model. *AIP Conference Proceedings*,
- Shen, F., Münstermann, S., & Lian, J. (2020). An evolving plasticity model considering anisotropy, thermal softening and dynamic strain aging. *International Journal of Plasticity*, 132, 102747. <https://doi.org/https://doi.org/10.1016/j.ijplas.2020.102747>
- Sahoo, Bibhuti & Sankalp, Sovan & Kisi, Ozgur. (2023). A Novel Smoothing-Based Deep Learning Time-Series Approach for Daily Suspended Sediment Load Prediction. *Water Resources Management*. 37. 1-22. 10.1007/s11269-023-03552-7.

Appendix

1. Temperature dependent parameter calibration

Seven-parameter temperature dependency functions:

$$f(T, \varepsilon) = \frac{\sigma_T}{\sigma_{RT.QS}} = C_1(\varepsilon) \cdot \exp(-C_2(\varepsilon) \cdot T) + C_3(\varepsilon) \quad (\text{A-1})$$

$$+ C_4(\varepsilon) \cdot \exp \left[- \left(\frac{T - C_5(\varepsilon) - C_7}{C_6(\varepsilon)} \right)^2 \right]$$

$$f(T, \varepsilon) = \frac{\sigma_T}{\sigma_{RT.QS}} = C_1(\varepsilon) \cdot \exp(-C_2(\varepsilon) \cdot T) + C_3(\varepsilon) \quad (\text{A-2})$$

$$+ C_4(\varepsilon) \cdot \exp \left[-C_7 * \left(\frac{T - C_5(\varepsilon) - C_7}{C_6(\varepsilon)} \right)^2 \right]$$

Where:

- C_7 is an additional parameter compared with the six-parameter function.

Table A-1

The r-squared value of prediction curves at different strain-rates of the seven-parameter function (A-1).

| R-squared / Strain-rate | 0.0001 | 0.001 | 0.01 | 0.1 |
|-------------------------|--------|--------|--------|--------|
| Smallest value | 0.971 | 0.685 | 0.870 | 0.897 |
| Largest value | 1 | 1 | 1 | 1 |
| Average value | 0.994 | 0.998 | 0.997 | 0.998 |
| R-squared values > 0.99 | 99.75% | 98.99% | 88.61% | 94.84% |

Table A-2

The r-squared value of prediction curves at different strain-rates of the seven-parameter function (A-2)

| R-squared / Strain-rate | 0.0001 | 0.001 | 0.01 | 0.1 |
|-------------------------|--------|--------|--------|-------|
| Smallest value | 0.971 | 0.705 | 0.87 | 0.897 |
| Largest value | 1 | 1 | 1 | 1 |
| Average value | 0.994 | 0.998 | 0.991 | 0.998 |
| R-squared values > 0.99 | 99.75% | 98.09% | 84.56% | 96.2% |

Table A-3

Calibrated thermal parameters of six-parameter function at different strain values at strain-rate 0.0001

| Strain | C1 | C2 | C3 | C4 | C5 | C6 |
|---------|------|------|------|------|--------|--------|
| 0.00011 | 3.00 | 0.01 | 0.74 | 0.73 | 527.46 | 183.46 |
| 0.0003 | 2.86 | 0.01 | 0.18 | 0.93 | 514.82 | 350.00 |
| 0.0005 | 2.60 | 0.01 | 0.30 | 0.79 | 508.65 | 350.00 |
| 0.002 | 1.85 | 0.01 | 0.37 | 0.64 | 524.55 | 350.00 |
| 0.004 | 1.49 | 0.01 | 0.47 | 0.48 | 546.28 | 294.46 |
| 0.01 | 1.64 | 0.00 | 0.15 | 0.66 | 586.16 | 314.89 |
| 0.03 | 1.69 | 0.00 | 0.00 | 0.63 | 597.60 | 270.46 |
| 0.05 | 1.69 | 0.00 | 0.00 | 0.62 | 594.70 | 256.20 |
| 0.3 | 2.02 | 0.00 | 0.00 | 0.88 | 576.40 | 297.02 |
| 0.5 | 2.23 | 0.01 | 0.00 | 0.98 | 564.74 | 318.15 |
| 0.6 | 2.32 | 0.01 | 0.00 | 1.00 | 560.00 | 325.86 |

Table A-4

Calibrated thermal parameters of nine-parameter function at different strain values at strain-rate 0.0001

| Strain | C1 | C2 | C3 | C4 | C5 | C6 | C7 | C8 | C9 |
|---------|------|-------|------|------|--------|--------|------|--------|--------|
| 0.00011 | 3.32 | 0.005 | 3.57 | 0.37 | 400 | 69.58 | 1.22 | 582.11 | 200 |
| 0.0003 | 2.47 | 0.01 | 0.75 | 0.05 | 398.01 | 63.42 | 0.45 | 519.90 | 193.25 |
| 0.0005 | 2.07 | 0.01 | 0.71 | 0.09 | 324.05 | 50 | 0.39 | 517.44 | 200 |
| 0.002 | 1.53 | 0.01 | 0.81 | 0.05 | 298.20 | 50.13 | 0.23 | 506.20 | 183.27 |
| 0.004 | 1.25 | 0.01 | 0.90 | 0.07 | 336.68 | 51.95 | 0.16 | 516.43 | 86.13 |
| 0.01 | 1.07 | 0.09 | 0.90 | 0.06 | 342.53 | 55.23 | 0.29 | 522.41 | 50.1 |
| 0.03 | 0.95 | 0.01 | 0.90 | 0.04 | 351.05 | 51.32 | 0.24 | 525.57 | 60.44 |
| 0.05 | 1.16 | 0.00 | 0.55 | 0.03 | 332.53 | 60.27 | 0.37 | 562.36 | 188.43 |
| 0.3 | 1.79 | 0.01 | 0.57 | 0.31 | 368.17 | 196.29 | 0.42 | 592.58 | 151.86 |
| 0.5 | 2.03 | 0.01 | 0.53 | 0.34 | 359.88 | 169.35 | 0.51 | 589.75 | 159.35 |
| 0.6 | 1.78 | 0.01 | 0.73 | 0.15 | 343.59 | 93.36 | 0.4 | 552.11 | 149.48 |

Table A-5

Calibrated parameters in the thermal parameter equation for the six-parameter function at strain-rate 0.0001

| Parameters | C1 | C2 | C3 | C4 | C5 | C6 |
|------------|---------|---------|----------|--------|---------|----------|
| Q_1 | -11.311 | 0.000 | 0.500 | 0.225 | -94.874 | 81.628 |
| Q_2 | 0.009 | 0.019 | 0.004 | -0.012 | -0.001 | 0.003 |
| Q_3 | 0.009 | 0.004 | -0.003 | 0.029 | -0.005 | 0.018 |
| P_1 | 8.059 | 0.008 | 1.429 | -0.436 | 195.922 | -184.885 |
| P_2 | 202.742 | 190.618 | 8967.808 | 5.034 | 5.442 | 1.760 |
| M_1 | 0.245 | 0.001 | -0.073 | 0.682 | 35.530 | 28.696 |
| M_2 | 0.097 | 0.741 | 1.907 | 1.947 | -0.113 | 1.605 |
| M_3 | 0.271 | -0.316 | 0.498 | 2.280 | 1.087 | 0.403 |
| N_1 | 3.033 | 0.010 | 0.544 | 0.453 | 525.528 | 664.257 |
| N_2 | 2.158 | 1.682 | 4.217 | -4.965 | 7.793 | 0.348 |

2. Strain-rate dependent parameter calibration

Table A-6

Calibrated strain-rate parameters of C_1 function at different temperatures.

| | 298.15K | 373.15K | 473.15K | 573.15K | 673.15K |
|-------|----------------|----------------|----------------|----------------|----------------|
| a_1 | -0.330 | -2.962 | -0.824 | -1.183 | -0.185 |
| b_1 | -9515.448 | -4339.483 | -32112.415 | -11147.807 | -5495.783 |
| c_1 | 0.001 | 1.820 | 0.350 | -0.221 | -0.194 |
| d_1 | 194297.601 | 1663251.15 | 1125580.08 | -200775.390 | 111897.531 |
| e_1 | -275.853 | -3643.534 | -1618.484 | 455.096 | -57.451 |
| a_2 | -77.442 | 5.705 | 0.702 | 0.112 | 29.563 |
| b_2 | -180.287 | -161.595 | -0.201 | -17.986 | 0.007 |
| c_2 | 0.071 | -0.176 | -0.905 | -0.207 | -29.504 |
| a_3 | -0.109 | 0.306 | 0.123 | -0.404 | 0.000 |
| b_3 | 358.695 | -252.347 | -26.685 | 302.675 | -507.012 |

| | | | | | |
|-------|---------|---------|---------|---------|----------|
| c_3 | -5.143 | -0.739 | -1.183 | -3.262 | 13.150 |
| d_3 | 68.007 | 72.296 | -59.208 | 245.186 | -189.742 |
| e_3 | 465.432 | -68.556 | 447.497 | 80.244 | 267.064 |
| g_3 | -24.224 | -3.438 | 4.484 | -6.123 | -7.542 |

Table A-7

Calibrated strain-rate parameters of C_2 function at different temperatures.

| | 298.15K | 373.15K | 473.15K | 573.15K | 673.15K |
|-------|----------------|----------------|----------------|----------------|----------------|
| a_1 | -0.290 | -0.525 | 0.015 | -0.179 | -1675088.55 |
| b_1 | 616.643 | 19.329 | -4.869 | 7.902 | -872.069 |
| c_1 | 1.220 | 0.081 | 0.555 | 0.079 | 138.118 |
| d_1 | -0.985 | -13.397 | 1.562 | -4.929 | -12505132 |
| a_2 | -0.032 | -0.996 | -0.032 | 0.035 | 0.591 |
| b_2 | 0.294 | 10.102 | 13884.337 | 128.282 | -1.149 |
| c_2 | 0.275 | 0.289 | 4.014 | 2.781 | 4.693 |
| d_2 | 0.843 | -6.317 | 1.164 | 1.198 | 6.457 |
| a_3 | -0.095 | 0.400 | -0.319 | -0.133 | -0.523 |
| b_3 | 0.815 | -1.000 | 3.166 | 1.603 | 1.640 |
| c_3 | 0.409 | 0.423 | 0.371 | 0.396 | -0.231 |
| d_3 | 0.530 | 2.752 | -0.760 | 0.189 | -3.170 |

Table A-8

Calibrated strain-rate parameters of C_3 function at different temperatures.

| | 298.15K | 373.15K | 473.15K | 573.15K | 673.15K |
|-------|----------------|----------------|----------------|----------------|----------------|
| a_1 | -608701307 | -302750547 | 633581498 | 229294240 | -7659953480 |
| b_1 | 1935615.05 | 573678.86 | -2170117.34 | -772858.029 | 24613178.200 |
| c_1 | -1769.869 | 467.217 | 2134.776 | 768.384 | -21172.796 |
| d_1 | 0.602 | -0.395 | -0.338 | -0.408 | 5.182 |
| a_2 | -5795.189 | -81719.094 | 4550.946 | 19251.733 | 3368.637 |
| b_2 | -29.626 | 6048.726 | -309.265 | -1577.479 | -560.190 |
| c_2 | 13.990 | -124.687 | 5.379 | 42.933 | 13.171 |
| d_2 | -0.154 | 0.711 | 0.344 | -0.230 | 0.068 |

| | | | | | |
|-------|--------|---------|-------|--------|--------|
| a_3 | 30.378 | -34.917 | 2.995 | -7.505 | 17.546 |
| b_3 | -4.742 | 5.123 | 0.388 | 2.150 | -2.920 |
| c_3 | 0.104 | 0.09 | 0.331 | 0.107 | 0.022 |

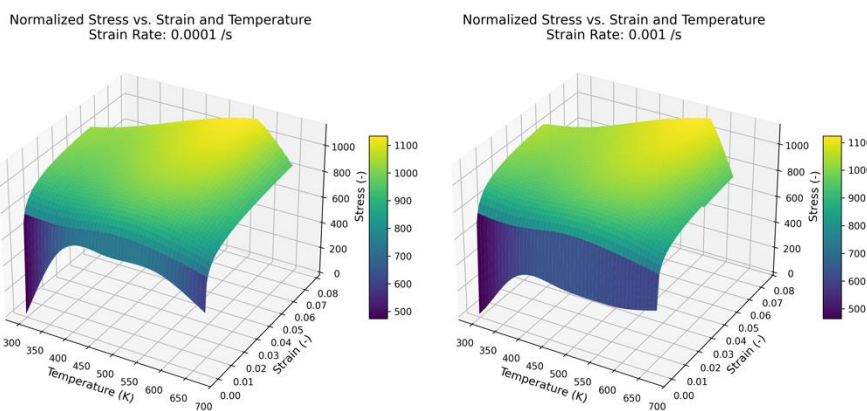
Table A-9

Calibrated strain-rate parameters of C_4 function at different temperatures.

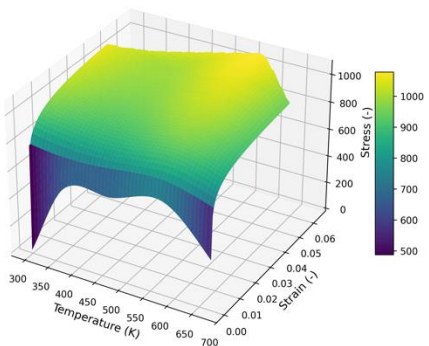
| | 298.15K | 373.15K | 473.15K | 573.15K | 673.15K |
|-------|----------------|----------------|----------------|----------------|----------------|
| a_1 | -0.021 | -0.198 | -0.231 | -0.227 | -0.022 |
| b_1 | -9097.829 | -5694.633 | -10496.779 | -6485.096 | -1067.343 |
| c_1 | -11324.407 | 2014.001 | -7734.323 | -0.050 | 0.014 |
| d_1 | -0.002 | -0.007 | -0.009 | -0.036 | 0.001 |
| a_2 | 0.023 | -1.248 | -0.000 | -0.419 | -1.022 |
| b_2 | -31.091 | 0.003 | 11.859 | 0.117 | 0.136 |
| c_2 | -0.008 | 1.24 | -0.010 | 0.415 | 1.024 |
| a_3 | -0.008 | 0.006 | 1.198 | 0.025 | 0.016 |
| b_3 | -373.047 | 515.5 | -18.377 | -321.400 | -0.021 |
| c_3 | 3.931 | -9.200 | 1.311 | 5.363 | -6.439 |
| d_3 | 135.505 | 78.279 | -4.585 | 333.831 | -70.807 |
| e_3 | 2.722 | -10.955 | 232.432 | 1.452 | 34.739 |
| f_3 | -0.068 | 0.426 | 0.032 | -0.176 | -0.411 |
| g_3 | -0.002 | -0.009 | -1.169 | -0.002 | 0.002 |

3.

Figure 1. 3D Plots of experimental data



Normalized Stress vs. Strain and Temperature
Strain Rate: 0.01 /s



Normalized Stress vs. Strain and Temperature
Strain Rate: 0.1 /s

